Research Square

Preprints are preliminary reports that have not undergone peer review.
They should not be considered conclusive, used to inform clinical practice,
or referenced by the media as validated information.

CFD Model Predictions of Zero Boil-Off Unvented and Vented Tank Filling in Microgravity

Rebecca L. Winter

rebecca.l.winter@nasa.gov

Case Western Reserve University

Mohammad Kassemi

Case Western Reserve University

Research Article

Keywords: Cryogenic Fluid Management (CFM), two-phase flow, no-vent tank filling, cryogenics, microgravity physics, Computational Fluid Dynamics (CFD) modeling.

Posted Date: July 3rd, 2026

DOI: https://doi.org/10.21203/rs.3.rs-9943653/v1

License: This work is licensed under a Creative Commons Attribution 4.0 International License.
Read Full License

Additional Declarations: No competing interests reported.

Version of Record: A version of this preprint was published at Microgravity Science and Technology on October 31st, 2026. See the published version at https://doi.org/10.1007/s12217-026-10295-8.

1 Title

CFD Model Predictions of Zero Boil-Off Unvented and Vented Tank Filling in Microgravity

2 Author Information

2.1 Authors and Affiliations

Rebecca L. Winter

National Center for Space Exploration Research (NCSER), Case Western Reserve University, NASA Glenn Research Center, Cleveland, OH, USA

ORCID: 0000-0003-2896-3848

Mohammad Kassemi

National Center for Space Exploration Research (NCSER), Case Western Reserve University, NASA Glenn Research Center, Cleveland, OH, USA

ORCID: 0009-0005-7983-276X

2.2 Corresponding Author

Rebecca L. Winter

Email: rebecca.l.winter@nasa.gov

3 Abstract

Cryogenic Fluid Management (CFM) of propellant fluids in microgravity presents an important challenge for NASA's future long-duration space missions, which will require safe and efficient storage and transfer of cryogenic liquid fuels. The Zero-Boil-Off Tank Filling and Transfer Experiment (ZBOT-FT) or Transfer and Refilling Experiment (TREX), through collaboration between the University of Bremen and Case Western Reserve University, aims to study two-phase tank-to-tank transfer operations in microgravity using the simulant fluid Perfluoro-n-pentane (PNP). As part of this effort, this work presents two-phase Computational Fluid Dynamics (CFD) models for no-vent and vented cylindrical tank filling operation in microgravity for filling rates of 1.0-1.65 mL/s. 2D axisymmetric and 3D parametric CFD simulation case studies are performed to show the detailed physics and evolution of tank pressure. A zero-dimensional homogeneous thermodynamic model is developed to predict the final steady-state pressure.

The CFD models demonstrate two stable geyser behaviors (low stable geyser and wobbly geyser) and two unstable behaviors (droplet shedding and jet column). When Weber number is adjusted for inlet velocity profile, a threshold between 1.5 and 1.7 divides stable and unstable regimes, consistent with previous experimental findings. The final pressure in the CFD models converges to the thermodynamic limit. 2D and 3D results show broad agreement for most cases, though 3D modeling is required for wobbly geyser cases. The models show that geyser behavior significantly affects the early transient pressure evolution, with stable geyser cases displaying higher pressure peaks, and suggests that lower fill rates may sometimes result in higher peak pressure.

4 Keywords

Cryogenic Fluid Management (CFM); two-phase flow; no-vent tank filling; cryogenics; microgravity physics; Computational Fluid Dynamics (CFD) modeling.

5 Statements and Declarations

5.1 Competing Interests

The authors have no competing interests to declare.

5.2 Author Contributions

All authors contributed to the study conception and design. Material preparation, data collection, and analysis were performed by Rebecca L. Winter and Mohammad Kassemi. The first draft of the manuscript was written by Rebecca L. Winter, and all authors commented on previous versions of the manuscript. All authors read and approved the final manuscript.

5.3 Data Availability Statement

The data generated during and/or analyzed during the current study are available from the corresponding author on reasonable request.

6 Acknowledgments

Funding and programmatic support from the Microgravity Biological and Physical Sciences (BPS) Division at NASA Headquarters through the Zero-Boil-Off Tank Filling & Transfer (ZBOT-FT) Experiment under the contract number 80GRC020D0003 are gratefully acknowledged. The authors also acknowledge the collaborative efforts of the Dr. Sesha Govindan, Prof. Michael Dreyer, and the Multiphase Flow Group at ZARM and the University of Bremen in support of the Zero-Boil-Off Tank Filling and Transfer Experiment/Transfer and Refilling Experiment (ZBOT-FT/TREX) project.

7 Introduction

In-orbit refueling of propellant liquid is vital to NASA's goal of future long-duration space missions. Without an adequate and efficient method of refueling in low gravity environments, each mission must carry with it all of the fuel essential from launch to return. NASA's plans for manned, long-duration space missions to the moon and to Mars are not feasible without the ability to refuel during the mission.

Implementation of a refueling system introduces numerous challenges and requires the study of Cryogenic Fluid Management (CFM) under low gravity conditions. An increase in pressure of the cryogenic liquid fuel, either due to heat leak in the system or the tank filling itself, can lead to pipe rupture or even self-ignition of the fuel. This can be averted by venting the fuel during refueling, however venting reduces the efficiency of the transfer.

A number of experimental and computational studies have been performed in the past decades to investigate the fundamental two-phase flow, heat transfer, and phase change aspects of vented and ventless tank filling in both 1g and microgravity. Symons et al (1968) studied tank filling in low gravity with a series of drop tower experiments using ethanol, butanol, and trichlorotrifluoroethane at a range of inlet velocities and inlet radii. They found that the Weber number based on inlet radius and inlet velocity could predict the stability of the geyser interface. This work was expanded to partially prefilled tanks by Symons (1969). Later, the effects of inlet flow profile were considered by Symons and Staskus (1971). Aydelott (1979) performed additional drop tower experiments with ethanol and identified four distinct geyser flow patterns for partially filled tanks, which were further discussed by Hochstein et al (2008).

Chato (1989) was among the first to perform a ventless tank filling experiment with liquid hydrogen (LH2). They showed the feasibility of the filling process for a cryogen in 1g, achieving a final fill level of 94%, and found that a top spraying configuration results in a better performance than a bottom spraying method. Moran et al (1990) carried out ventless tank filling experiments with liquid hydrogen and liquid nitrogen (LH2 and LN2) with a top-mounted full cone droplet spray injection nozzle. Their results indicated that no-vent fill of LN2 to fill levels above 90% is possible in 1g, though they found the ventless LH2 fills to be considerably harder to achieve than those with LN2. Three distinct regions of pressure variation were observed in the no-vent fill tests, and the pressure variation was mostly influenced by the incoming liquid temperature. First was an initial steep pressure increase as the incoming liquid quickly boiled against the warmer walls of the tank. Second, the pressure leveled off or even began to decrease as boiling reduced and condensation of the ullage vapor on the filling liquid increased. Finally, at very high fill levels exceeding 90%, they observed a sudden pressure rise as the liquid interface began to submerge the inlet nozzle.

Later, Moran et al (1991) performed another ground-based LH2 no-vent filling experiment using three different injection mechanisms of top-spray, upward pipe discharge, and bottom diffuser. More than 40 tests were performed with various liquid inlet temperatures, flow rates, and initial tank wall temperatures, with 40% of the tests achieving fill levels above 90%. The top-spray was again found to be the most efficient configuration in 1g by promoting enhanced condensation of the vapor during injection. Chato (1993) carried out another no-vent filling experiment with LH2, testing the performance of both a bottom orifice and an axial spraybar. Both inlet configurations achieved sufficient interaction between the liquid and vapor phases, resulting in favorable condensation rates to facilitate the filling process. He concluded that ground no-vent tank filling is achievable with various mechanisms and configurations.

Schmidt et al (1991) conducted 1g no-vent tank filling experiments using Freon-114, a transparent simulant fluid, and showed that a top-filling configuration achieves the highest fill levels because of significant liquid-vapor interface agitation. Subsequently, Vaughan et al (1991) and Vaughan and Schmidt (1991) extended the Freon-114 experiments by performing no-vent fills with different types of liquid inlet configurations and again recommended the top-filling configuration for achieving the best 1g performance. Chato and Sanabria (1991) performed a tank chilldown experiment to demonstrate that it is possible to sufficiently cool a tank for filling through a charge-hold-vent process. The method uses repeated injection of liquid droplets from top and bottom orifices followed by a hold period to allow complete vaporization of the liquid. It is terminated by venting the vapor to vacuum to cool the tank to the desired temperature. They showed that six charge-hold-vent cycles using 32 pounds of LH2 were sufficient to cool the tank from 440 R to below 100 R to subsequently allow a complete ventless fill of the test tank.

Flachbart et al (2002) performed fourteen LH2 tank filling tests to demonstrate the concept of on-orbit refilling of the Shuttle Upper Stage tank. They demonstrated rapid tank filling within 300 seconds, but ventless filling was not achieved due to insufficient precooling. Wang and Wang (2010) found that a cylindrical tank performed better in horizontal configuration than in vertical configuration under similar conditions in 1g due to an increased surface area that enhances condensation mass transfer. Finally, Wang et al (2011) performed a 1g experiment with LN2 to compare tank filling under vented and ventless conditions and found the temperatures, pressures, and phase change behaviors of the two systems to be significantly different. In ventless filling, three distinct pressurization behaviors were noted, as previously observed by Moran et al (1990), namely fast pressure increase, tapering and slow pressure decrease, and sharp pressure rise at the end. In the vented case, the pressure evolution indicated only two distinct segments during the filling process and did not show the final sharp pressure rise.

Vented and ventless tank filling has also been subjected to various theoretical and computational treatments, including simple thermodynamic analyses by homogeneous models, more complicated system-level computations via multizone or nodal models, and elaborate two-phase simulations using CFD codes. Gille (1986) analyzed the ventless transfer of cryogenic liquids using a thermodynamic model and was able to show the sensitivity of the filling process to the fluid properties and tank size. These computations also confirmed that lower temperature liquids such as LH2 are harder to transfer. Chato (1988) used the NVFILL (No-Vent Fill) model to solve the no-vent filling problem following a two-stage analysis. In the first stage, the initial liquid flash evaporation upon injection of the liquid was captured by a thermodynamic model, while the subsequent ullage condensation and compression in the second stage were solved using a three-node model representing the liquid, gas, and interface domains. This model was later improved by Taylor and Chato (1991) to capture the partial vaporization of a liquid as it enters the tank and the bulk liquid heating. The results from the improved model were validated against the experimental data obtained by Moran et al (1990). Ma et al (2023) developed a four-node model for no-vent liquid hydrogen filling in microgravity that allows for more rapid parametric studies of no-vent filling performance.

Vaughan and Schmidt (1991) developed the FILL code to analytically model the no-vent fill process under normal gravity conditions. It was shown that the transient behavior of the state properties predicted by the analytical model was in good agreement with the test data. Furthermore, the condensation rates calculated from the FILL model also matched well with the theoretical submerged jet prediction. Later the FILL Model was enhanced and validated against the Freon-114 ventless fill data by Vaughan and Schmidt (1991), confirming its ability to predict ventless filling performance in 1g. The code was also used to validate existing empirical condensation correlations used in system level simulations. Honkonen et al (1991) developed the General Dynamics No-Vent Fill program (GDNVF) for capturing tank chilldown and no-vent filling process. When compared against ground-based LH2 data for a cylindrical tank, the results matched the experimental tank pressure evolution but overpredicted the initial pressure rise. Taylor and Chato (1992) developed an improved thermodynamic equilibrium model and validated it against the results of their 4.96 m3 LH2 no-vent filling experiment. They found that this model provided a better prediction of the experimental results compared to their previous droplet heat transfer NVFILL model. Majumdar (2013) modelled the no-vent chill and fill process of a liquid hydrogen tank using the Generalized Fluid System Simulation Program (GFSSP) tool. The charge-hold-vent process was simulated using nodal models. The nodal models were validated with the K-site test data, and it was found that the models provided good predictions of the propellant consumption and chilldown time.

Marchetta and Benedetti (2010) developed a 2-dimensional CFD axisymmetric model using RIPPLE and a 3-dimensional CFD model using ANSYS Fluent of filling of partially filled tanks. They compared the performance of the simulations using different turbulence modeling schemes to experimental results. They found that the RIPPLE simulations with the k-ε turbulence modeling provides the most accurate results when compared with experiments from Aydelott (1979).

Wang et al (2015) developed and used two system-level finite difference models to make a comparative study of the 1g and microgravity performances of the LH2 ventless filling process. A series of heat transfer mechanisms such as film boiling, transition boiling, nucleate boiling, and liquid natural convection were considered to capture the fluid wall heat transfer accurately. The simulations indicated that in 1g, the tank experiences a continuous pressure rise during the whole filling process such that the highest pressure is reached at the end of the operation. In microgravity,

however, the maximum pressure occurs at the beginning of the filling process. They also showed the different sensitivities of the 1g and microgravity filling performance to variations in the inlet mass flux, inlet liquid temperature, and wall temperature. Ma et al (2017) developed a CFD model for no-vent filling of a liquid hydrogen tank and validated it against data from ground experiments performed by Moran et al (1991). They performed 1g and microgravity simulations and showed that the pressure evolution in both 1g and microgravity filling cases go through the three distinct rate changes shown previously. The simulations also indicated that the inlet configuration had negligible impact on the ventless filling in microgravity since under weightlessness, the liquid jet easily reaches the tank wall to cool it down and vapor-liquid mixing is enhanced. Thus, the simulations indicate that the pressure response in microgravity is steadier than in 1g, rendering better microgravity filling performance compared to its ground-based counterpart. Kartuzova and Kassemi (2017) performed two-phase CFD simulations based on the K-site charge-hold-vent chill and fill LH2 experiment conducted by Chato and Sanabria (1991). The simulations used an in-house developed conjugated storage tank CFD model in the framework of the ANSYS Fluent CFD code. A discrete particle Eulerian-Lagrangian approach together with an in-house developed droplet phase change model were used to track the spray droplets and capture the heat and mass transfer interactions between the discrete droplets and the continuous ullage phase. The predicted tank pressure and temperature evolutions at different fluid and wall measurement locations were validated against the experimental results. The CFD predictions agreed reasonably well with the experimental pressure, however the average tank wall temperature was over-predicted in the CFD simulations. This may be because liquid film formation and flash evaporation on the tank wall were not included in the model during the charge-hold-vent simulations.

Dominick and Driscoll (1993) reported the first microgravity filling data that was generated by the vented fill tests conducted as part of the Fluid Acquisition and Resupply Experiment (FARE) on-board the space shuttle. In FARE-I, the spherical tank contained a screen channel propellant management device (PMD) and final fill levels of 60% to 80% were achieved during the vented fill tests. In the FARE-II experiment, reported by Dominick and Tegart (1994), a vane-type acquisition device was used. An abrupt transition from stable to unstable flow was observed during the vented fill tests but final fill levels of greater than 95% were routinely achieved without losing any liquid because the vanes kept the liquid settled.

The Vented Tank Resupply Experiment (VTRE), reported by Chato and Martin (2006), demonstrated successful transfer of refrigerant 113 between two spherical tanks at different flow rates and liquid-free venting. More recently, the vented filling of a partially filled tank in reduced gravity was investigated experimentally by Govindan and Dreyer (2023) in the Bremen 10 second Drop Tower facility. Experiments were performed with HFE-7500 simulant fluid under 9 seconds of reduced gravity. Subcritical, critical, and supercritical jet flow regimes were identified at different filling flow rates from 1.10 mL/s to 1.50 mL/s. Experiments were classified into stable and unstable liquid interfaces, and the critical Weber number for initiation of liquid geyser interface instability was found to be around 1.04.

The jet-ullage interactions that occur during jet mixing in ventless tank filling were subject to microgravity investigations using simulant fluids in the Tank Pressure Control Experiment (TPCE) aboard the Space Shuttle, as reported by Bentz et al (1997), and in the Zero-Boil-Off Tank (ZBOT) experiment performed on the International Space Station (ISS), as reported by Kassemi et al (2018). Microgravity data from both experiments were used to validate the predictions of a two-phase CFD model for tank pressurization and pressure control, developed as part of the ZBOT investigation with good success, as reported by Kartuzova and Kassemi (2019; 2024).

In the present work, we study the behavior of a filling tank in microgravity with both thermodynamic and CFD modeling approaches. We have developed a system level 0-dimensional thermodynamic model for predicting the overall behavior of the filling tank problem, and we compare its predictions to the CFD results. We present both 2-dimensional axisymmetric and 3-dimensional CFD simulations of no-vent tank filling in microgravity for different flow rates and flow profiles, with a specific focus on the pressure and mass transfer over time, as well as the liquid geyser behaviors. The 3D CFD model is also used to compare unvented and vented tank filling in microgravity, as well as the effects of initial tank fill condition and gravity condition. Previous experimental results from literature are used for model validation.

8 Thermodynamic Model

The thermodynamic model gives a simplified theoretical understanding of the no-vent filling problem by removing all spatial variations and geometry effects within the system. The model assumes homogeneity of the fluid in the tank at saturation temperature and pressure. Mass and energy conservation equations are solved and combined into a final generalized evolution equation given here.

$$\frac{dT}{dt} = \frac{\dot{Q}_W + h_{LV}\left(\dot{M}_{V,IN} - \dot{M}_{V,OUT}\right) + \frac{h_{LV}\rho_V}{\rho_L - \rho_V}\left(\dot{M}_{IN} - \dot{M}_{OUT}\right) + \left(c_{pV}\dot{M}_{V,IN} - c_{pL}\dot{M}_{L,IN}\right)(T_{IN} - T)}{c_{pV}\rho_V V_V + c_{pL}\rho_L V_T + \frac{h_{LV}\rho_V}{\rho_L - \rho_V}\left(\rho_V \frac{d\rho_L}{dT} V_L - \rho_L \frac{d\rho_V}{dT} V_V\right) - V_T \frac{dP}{dT} + c_W M_W} \tag{1}$$

For the specific example presented in this work, the equation is simplified to the following form for a thermally insulated tank of volume $V_T = V_L + V_V$ at a spatially-uniform, time-dependent temperature T with a mass flow rate $\dot{M}_{IN}$ of liquid entering at a temperature T_{IN}.

$$\frac{dT}{dt} = \frac{h_{LV}\rho_V \dot{M}_{IN} - c_{pL}(\rho_L - \rho_V)\dot{M}_{IN}(T_{IN} - T)}{(\rho_L - \rho_V)\left(c_{pV}\rho_V V_V + c_{pL}\rho_L V_T\right) + h_{LV}\rho_V\left(\rho_V \frac{d\rho_L}{dT} V_L - \rho_L \frac{d\rho_V}{dT} V_V\right) - (\rho_L - \rho_V) V_T \frac{dP}{dT}} \tag{2}$$

This equation is used to solve for temperature iteratively in MATLAB. The resulting pressure and phase change mass transfer are discussed and plotted alongside CFD results in Section 10.2.

9 Numerical Methods

9.1 Model Setup and Governing Equations

The CFD models are developed and run in ANSYS Fluent. The models use the Volume of Fluid (VOF) scheme with explicit formulation, sharp interface tracking, and laminar fluid flow. A pressure-based solver is used with the Pressure-Implicit with Splitting of Operators (PISO) scheme for pressure-velocity coupling. Gradients are evaluated using a least-squares cell-based approach. Pressure and volume fraction spatial discretization use the PREssure STaggering Option (PRESTO!) and Compressive schemes, respectively.

Fluid flow and heat transfer are described with the following governing equations for continuity, Navier-Stokes, and energy.

$$\frac{\partial \rho}{\partial t} + \nabla(\rho v) = 0 \tag{3}$$

$$\frac{\partial}{\partial t}(\rho v) + \nabla(\rho v v) = -\nabla P + \nabla\left[\mu_{eff}(\nabla v + \nabla v^T)\right] + \rho g + F_{vol} \tag{4}$$

$$\frac{\partial}{\partial t}(\rho E) + \nabla\big(v(\rho E + P)\big) = \nabla\big(k_{eff}\nabla T\big) + S_h$$

(5)

The enthalpy carried across the interface associated with the latent heat of phase change is accounted through the source term S_h, while the mass transfer associated with phase change is given by the source term S_α as discussed below.

The VOF scheme solves the continuity equation based on volume fraction α in each cell as follows.

$$\frac{1}{\rho_L}\left[\frac{\partial}{\partial t}(\alpha_L\rho_L) + \nabla\cdot(\alpha_L\rho_L v_L) = S_\alpha\right]$$

(6)

where

$$\alpha_L + \alpha_V = 1$$

(7)

In the VOF scheme, field variables and properties are defined and solved as averaged quantities based on the local volume fraction in each cell as follows.

$$\rho = \alpha_V\rho_V + \alpha_L\rho_L\,, \qquad \mu_{eff} = \alpha_V\mu_{eff\,V} + \alpha_L\mu_{eff\,L}\,, \qquad k_{eff} = \alpha_V k_{eff\,V} + \alpha_L k_{eff\,L}$$

(8)

Similarly, energy and temperature are treated as mass-averaged variables in the system.

$$E = \frac{\alpha_L\rho_L E_L + \alpha_V\rho_V E_V}{\alpha_L\rho_L + \alpha_V\rho_V}$$

(9)

Phase change mass transfer is defined by the source term S_α in the continuity equation shown as Equation (6). It is defined based on the Shrage model with an accommodation coefficient σ_{acc} of 0.1 based on previous work and implemented with a user-defined function (UDF) developed by Kassemi and Kartuzova (2016; Kartuzova and Kassemi 2024).

$$S_\alpha = \dot{M}_{int}\cdot A_{int}$$

(10)

where

$$\left|\dot{M}_{int}\right| = \left(\frac{2\sigma_{acc}}{2-\sigma_{acc}}\right)\left(\frac{M_M}{2\pi R}\right)^{1/2}\left(\frac{P_{int}}{T_{int}^{1/2}} - \frac{P_V}{T_V^{1/2}}\right)$$

(11)

and

$$A_{int} = |\nabla \alpha_V|$$

(12)

Surface tension forces at the liquid-vapor interface are modeled by Continuum Surface Force modeling, which applies the following volume force as a source term in the momentum equation.

$$F_{vol} = \sigma_{LV} \frac{\rho \kappa_{int} \nabla \alpha_V}{(\rho_V + \rho_L)/2}$$

(13)

where ρ is the volume-averaged density defined in Equation (8) and κ_{int} is the surface curvature of the interface, defined as the divergence of the unit normal vector.

9.2 Fluid Properties

Perfluoro-normal-pentane (PnP, C5F12) is used as the fluid in this single-species system, with relevant properties given in Table 1. The density is obtained from the ideal gas law in the vapor phase and represented by the Boussinesq approximation in the liquid, while the other properties are assumed constant due to the small temperature differences experienced in this case. All properties given here are based on the Design Institute for Physical Properties (DIPPR) values at 253.18 K.

Table 1 Properties of PnP liquid and vapor at 253.18 K based on DIPPR database

Property	Liquid	Vapor
Density	Boussinesq, 1743.919 kg/m3	Ideal gas
Specific Heat	1131.825 J/kg K	692.049 J/kg K
Thermal Conductivity	0.0697077 W/m K	0.00729833 W/m K
Viscosity	9.0238E-4 kg/m s	9.5936E-6 kg/m s
Molar Mass	288.034 kg/kmol	288.034 kg/kmol
Thermal Expansion Coefficient	0.00171415 K-1	N/A (ideal gas)
Latent Heat	104,401 J/kg	
Surface Tension Coefficient	0.0140107 N/m	
Wall Contact Angle	0°	

9.3 Model Settings, Domain, and Mesh

All models are run in ANSYS Fluent version 21.1 unless otherwise noted. The tank domain has a height of 0.094 m, a radius of 0.03 m, and an inlet at the center of the bottom boundary with a radius of 0.002 m, which matches the dimensions of the ZBOT-FT tank used in the drop tower experiments in Govindan and Dreyer (2023).

In unassisted tank filling, the tank wall is initially at a high temperature and the tank walls are cooled by the subcooled fluid as it fills the tank. In assisted tank filling, the tank wall is initially cooled by broad area cooling, and the filling proceeds in a cold tank without wall boiling considerations. The future ZBOT-FT experiment will test both situations; in this work, we consider only the assisted cold wall situation where the tank walls are adiabatic.

Gravitational acceleration is set to 9.81E-6 m/s^2 in the direction opposite to the inlet flow to simulate microgravity conditions. The inlet is prescribed a mass flow rate between 1.0 and 1.65 mL/s with either a flat (plug flow) or parabolic (Poiseuille flow) inlet profile. The model is initialized with pure saturated PnP vapor in the tank at 283.18 K and 10,000 Pa. It is run with a time step size of 1E-4 seconds for a total of 9 seconds of flow time.

9.3.1 2D Axisymmetric Unvented Model

Figure 1 shows the domain (top right) and mesh (bottom right) of the 2D axisymmetric no-vent case alongside a schematic depicting the axisymmetric symmetry of the 2D domain (left). The 2D mesh is structured and uniform with an element size of 3E-4 m and contains 31,714 elements.

[Fig. 1 appears here]

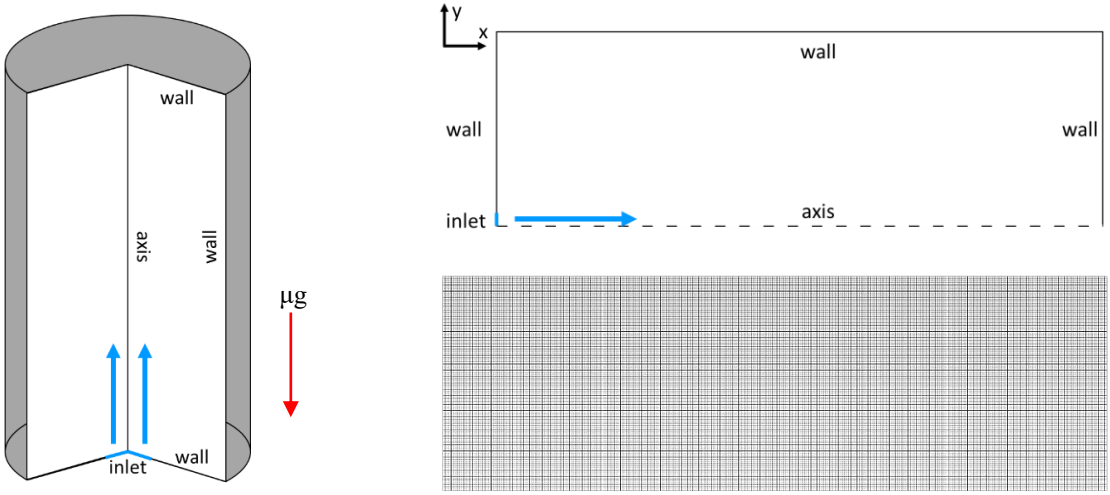


Figure 1 Schematics of 2D axisymmetric domain and image of corresponding mesh, with 31.7 thousand elements.

9.3.2 3D Unvented Model

The 3D mesh is unstructured polyhedral with refined regions in the center core and near the top and bottom walls, as shown in Figure 2. Regions of interest at the top and bottom walls and in the center core of the tank have element sizes of 3E-4 m while the remainder of the tank is prescribed an element size of 8E-4 m and an element growth rate of 1.2. ANSYS Meshing is used to make an initial tetrahedral mesh, which is then converted to a polyhedral mesh using Fluent. The final unvented mesh has 2,575,049 cells.

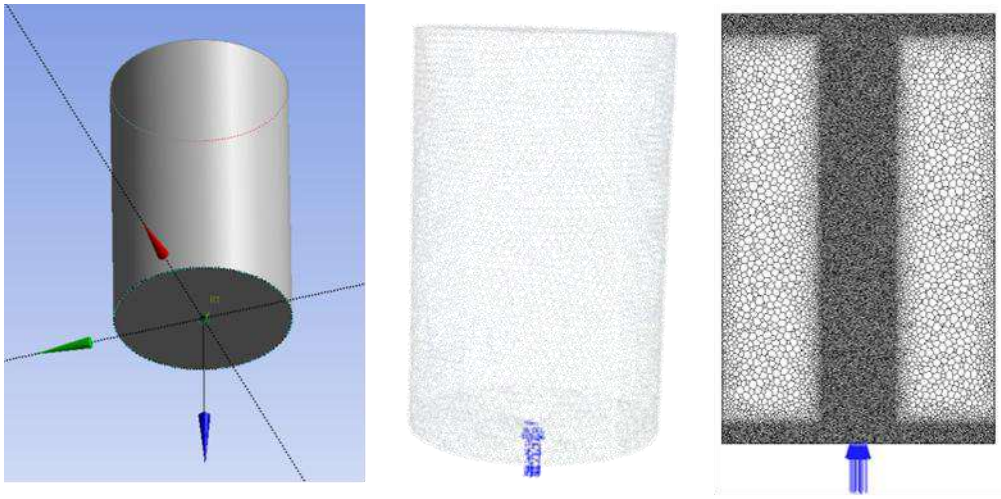


Figure 2 Images of 3D no-vent domain and center cross section of corresponding mesh, with a total of 2.6 million cells.

9.3.3 3D Side-Vented Model

The side-vented mesh has 2,604,568 cells and is shown with corresponding geometry in Figure 3. As in the 3D unvented model, the side-vented mesh is unstructured polyhedral with an element size of 8E-4 m and an element growth rate of 1.2 with refined regions of element size 3E-4 m in the center core and near the top and bottom walls. The vented geometry has an additional slit outlet around the tank circumferentially to vent the vapor.

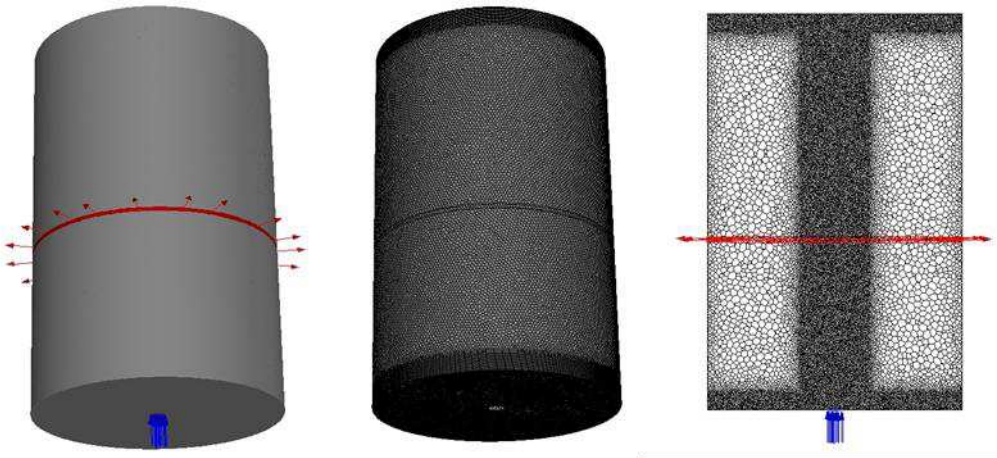


Figure 3 Images of 3D vented domain and center cross section of corresponding mesh, with 2.6 million cells.

9.3.4 3D Top-Vented Model

The top-vented model geometry and mesh are shown in Figure 4. A 1 mm radius top outlet is added to the 3D unvented base geometry, resulting in a top-vented mesh with 2,604,892 cells. The top-vented model is performed using ANSYS Fluent version 22.2 with a 1.4 mL/s filling flow rate.

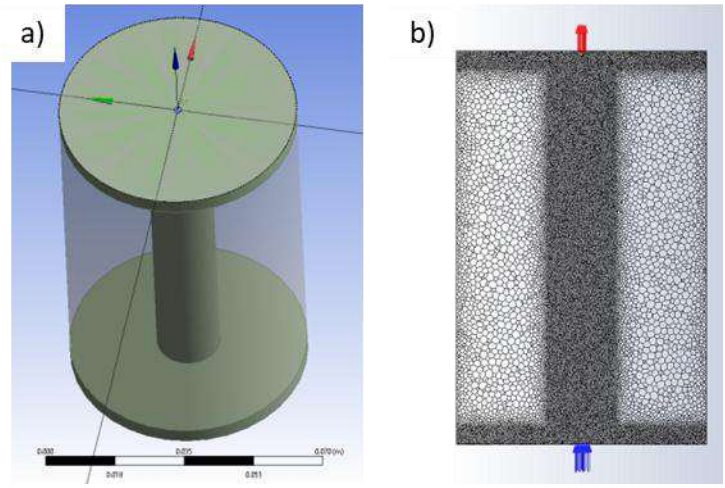


Figure 4 a) Geometry for top vent case showing the circular vent outlet at the top. b) Center cross section of the resulting mesh.

9.3.5 Earth Gravity and Zero-Gravity

The Earth gravity tank simulations are run on ANSYS Fluent version 21.2 with gravitational force set to 9.81 m/s2 in the direction opposite to the inlet flow, and for filling flow rates of 1.0 mL/s and 1.4 mL/s. The zero-gravity tank simulation is run on ANSYS Fluent version 23.1 with gravitational force disabled, and for filling flow rate of 1.0 mL/s. These cases are all run for 9 seconds of flow time with the same unvented mesh discussed in Section 9.3.2.

9.3.6 Partially Prefilled Tank

The unvented partially filled tank simulation is run with the tank initially filled to 10 mm with a filling flow rate of 1.4 mL/s. To better resolve the liquid interface for this case, the height of the refined region at the bottom of the tank is doubled to 20 mm. The resulting mesh has 4,588,723 cells and is shown in Figure 5. This case is run for 9 seconds of flow time on ANSYS Fluent version 22.2.

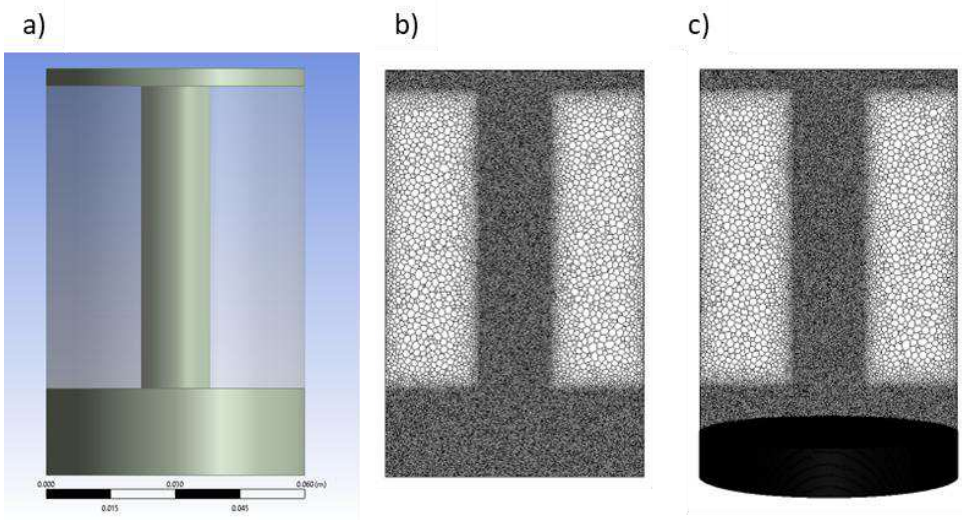


Figure 5 a) Geometry for partially filled tank case, with refined regions shown. b) Center cross section of the resulting mesh. c) Center cross section of the mesh with 3D surface of initially filled region shown in black.

9.3.7 Vacuum Tank Filling

The unvented evacuated tank filling simulation is run with the tank initially at a near vacuum with a filling rate of 1.4 mL/s It was found that the solution would not converge if the initial pressure was prescribed as 0 Pa, so an initial pressure of 100 Pa was used. This case is run for 30 seconds of flow time on ANSYS Fluent version 22.2 with the same unvented mesh discussed in Section 9.3.2.

9.4 3D Model Independence Studies and Optimization

9.4.1 Mesh Study

While finer meshes can allow for a more precise and refined solution, they are also more computationally expensive, particularly in 3D modeling. When the interface is captured by a VOF scheme, significantly increased mesh refinement at the interface also increases the Courant number, which can increase the spurious interfacial velocities and result in an undesirable overall solution. Therefore, a mesh study is performed to find the ideal mesh size for the problem.

Four unstructured uniform polyhedral meshes were studied initially at a flow rate of 1.4 mL/s. The center cross sections of these four meshes are shown at the top of Figure 6 with the corresponding liquid geyser shapes about halfway through the 9-second run shown at the bottom of Figure 6. In the two coarser meshes, the geyser appears to curve significantly. However, the geyser shape straightens out with a sufficiently refined mesh, suggesting that the curve is simply due to insufficient mesh refinement.

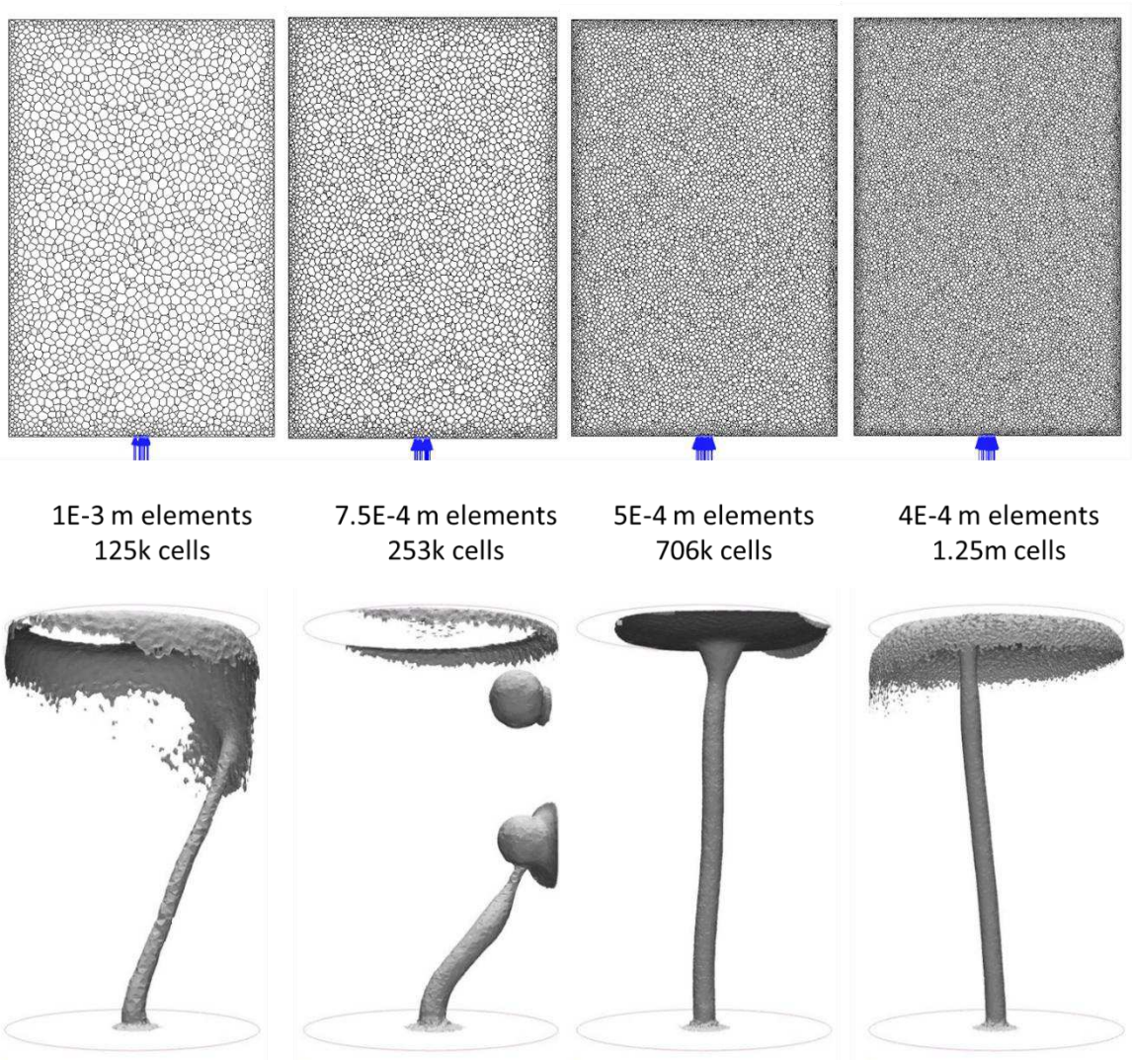


Figure 6 Top: Center cross sections of four uniform unstructured meshes with increasing refinement. Bottom: Resulting liquid geyser shape for each mesh at approximately t = 4.5 seconds for the 1.4 ml/s case.

If one assumes a straight geyser, then all the liquid-vapor interfaces are expected to be focused within the center core of the tank and along the top and bottom walls. In the set of meshes presented at the top of Figure 7, these most important regions of interest are more refined while the rest of the tank has a coarser mesh. This selective refinement keeps computational time more manageable while increasing refinement in the areas where it is most needed.

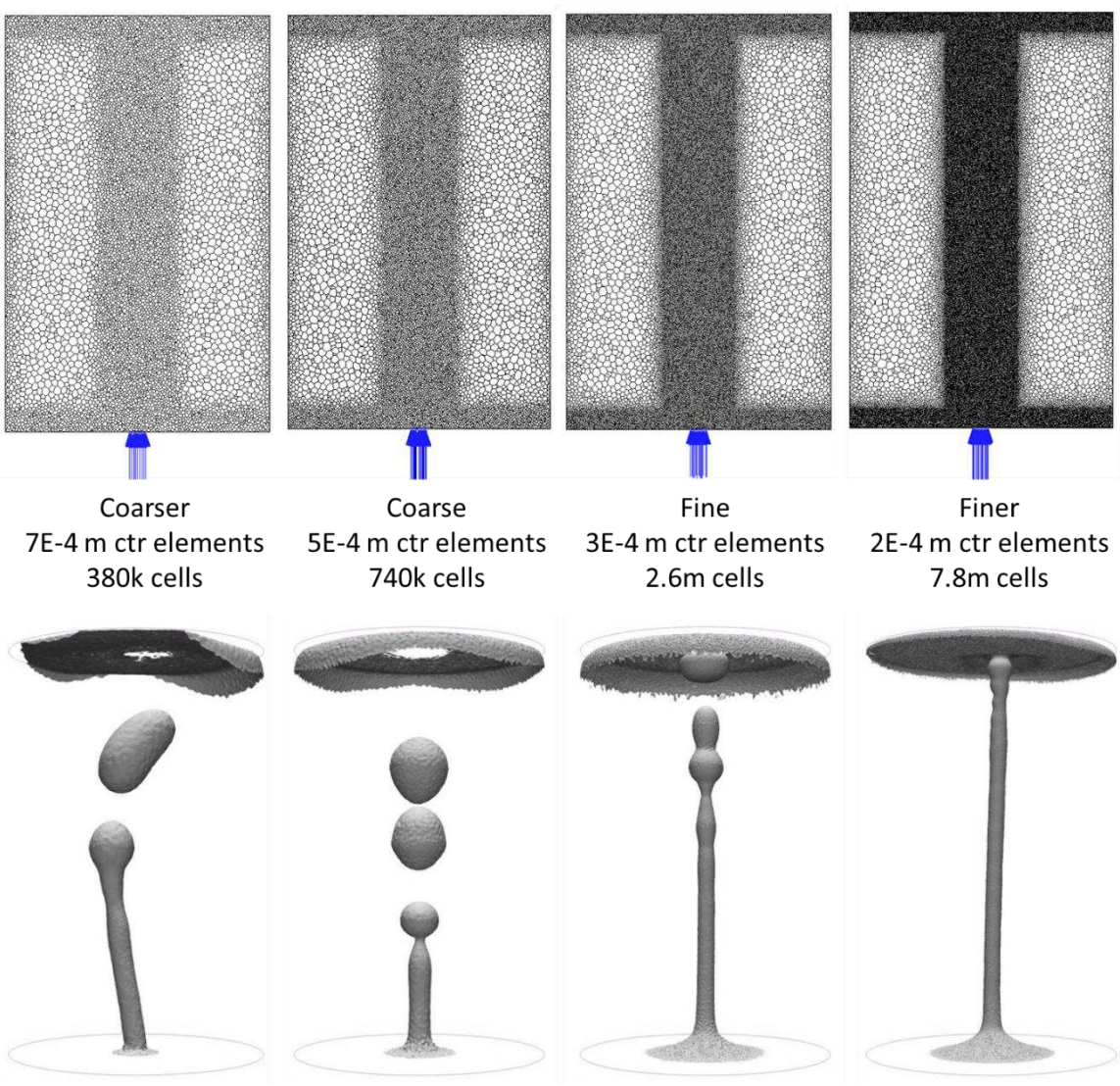


Figure 7 Top: Center cross sections of four non-uniform unstructured meshes with increasing refinement. Bottom: Resulting liquid geyser shape for each mesh at approximately t = 4.5 seconds for the 1.4 ml/s case.

As in Figure 6, Figure 7 shows cross sections of four meshes with varying levels of refinement and the corresponding liquid geyser shapes resulting from each mesh at ~4.5 seconds of flow time. As seen in the uniform meshes, the Coarser selectively refined mesh in Figure 7 also shows a curved geyser, so the Coarser mesh is eliminated from consideration.

Pressure and phase change mass transfer plots are shown in Figure 8 for each of the meshes in Figure 7. Thermodynamic results are also shown for comparison in Figure 8. Note that condensation is shown as negative phase change by convention in the plot. The figure demonstrates that both pressure and phase change have minimal dependence on the mesh, however, the Finer mesh shows some deviation in pressure. This may be due to spurious velocities that can become more pronounced with too much refinement. Therefore, the plots suggest that the 2.6 million cell Fine mesh is the optimal mesh for the model.

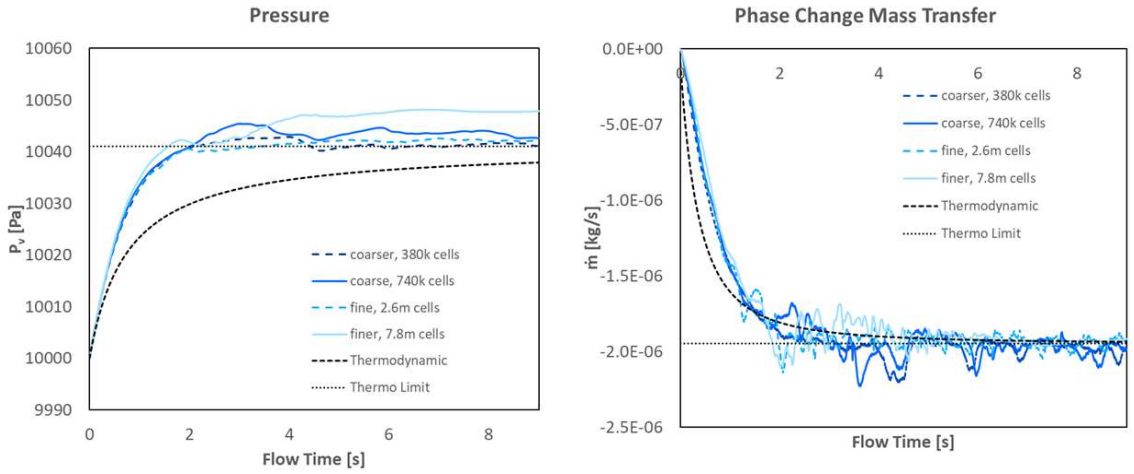


Figure 8 Plot of pressure in the vapor phase (left) and phase change mass transfer (right) as a function of time for four meshes. The thermodynamic results are included on both plots for comparison.

The pattern of droplet breakup of the geyser demonstrates some mesh dependence, as shown in the geyser snapshots at the bottom of Figure 7. This behavior can be further quantified by the breakup height in Figure 9, defined as the length of contiguous liquid measured from the inlet along the tank centerline. Three geyser shapes are shown to the right of the plot in Figure 9, one for each mesh shown in Figure 7 except the Coarser mesh, which has a curved geyser. Each geyser shape in Figure 9 is overlaid with a blue line indicating the measured breakup height for the specific snapshot. The plot on the left shows this breakup height, normalized by the total tank height, for these three cases at all times from 0 to 9 seconds. The 2.6 million cell Fine mesh, chosen based on the plots in Figure 8, also shows the most similar visual agreement with experimental geyser behavior from Govindan and Dreyer (2023).

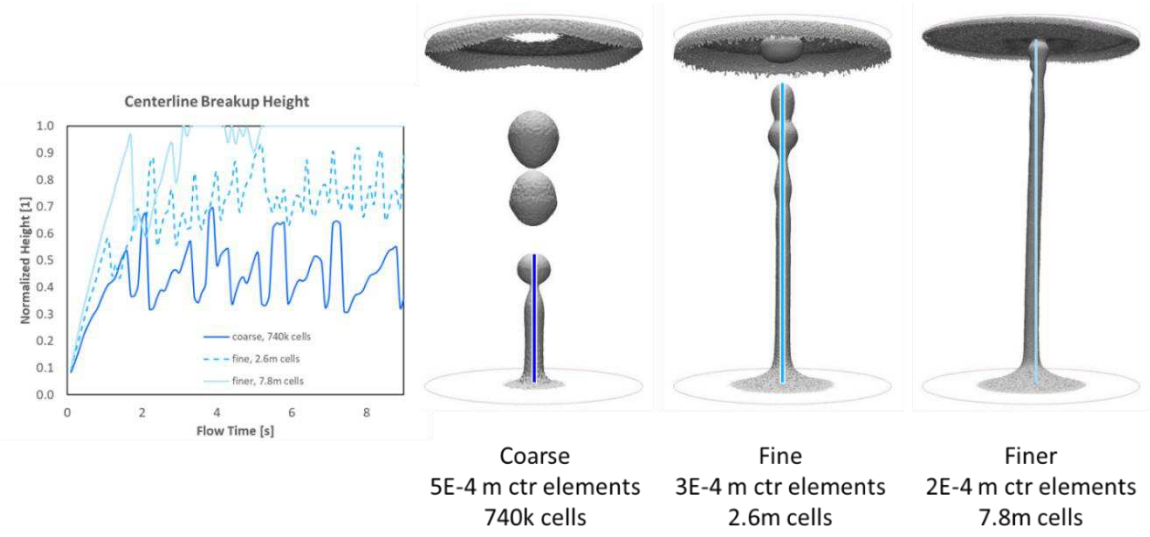


Figure 9 Left: Plot of centerline breakup height for three meshes. Right: Liquid geyser shape for each mesh at approximately t = 4.5 seconds with a line showing how the breakup height is measured.

9.4.2 Time Step Study

Similar to mesh refinement, the choice of time step size involves a balance between precision and computational cost, while also ensuring that the overall results and behavior of the model are largely independent of the time step size chosen. The 1.4 mL/s flow rate case is studied at a range of time step sizes varying from 5E-5 seconds to 1E-3 seconds. The results of this study are given in Figure 10, which shows plots of breakup height, pressure, and phase

change. The breakup height does display some dependence on time step size, with more breakup at smaller time step sizes. The mass transfer plot shows virtually no dependence on time step size. The pressure curves are nearly all the same, with a slight divergence of the smallest time step case (5E-5 seconds). This leads us to choose a time step size of 1E-4 seconds for the final model. The study suggests that while global factors of the problem such as pressure and mass transfer are largely time-independent, the interface breakup dynamics are sensitive to both the time step size and the mesh size.

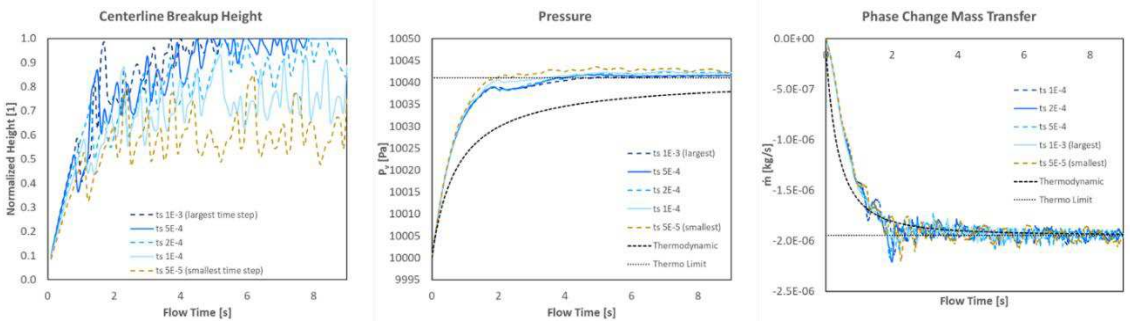


Figure 10 Plot of breakup height (left) for five time step sizes. See Figure 9 for a schematic showing how the breakup height is measured. Plot of pressure in the vapor phase (center) and phase change mass transfer (right) as a function of time for five time step sizes. The thermodynamic results are also plotted for comparison.

10 Results and Discussion

10.1 3D Model Geyser Behavior

Four major geyser patterns can be seen in the 3D CFD results for an unvented filling tank in microgravity, as shown in Figure 11 in order from lower to higher inlet velocities. The first is the low stable geyser, which shows a small liquid mound at the inlet and a steadily growing liquid level throughout inlet side of the tank. This shape characterizes the lowest inlet velocities and filling rates, and it yields the smallest liquid-vapor interfacial area of the four geyser shapes. The second is the wobbly geyser and is also considered a stable geyser shape. These cases begin with a small liquid geyser that initially grows straight above the inlet but begins to lean and bend erratically in different directions about the center as the tank fills. Droplet shedding behavior is shown in Figure 11c. In these cases, the geyser grows straight until it reaches a critical length where the liquid pinches off into a droplet, which continues to move toward the other side of the tank and impinge the opposite tank wall. As the droplets move, they sometimes coalesce with each other, as occurred shortly before the snapshot shown in the figure. Finally, Figure 11d shows a full jet column, in which the geyser reaches from the inlet to the opposite tank wall without breaking into droplets.

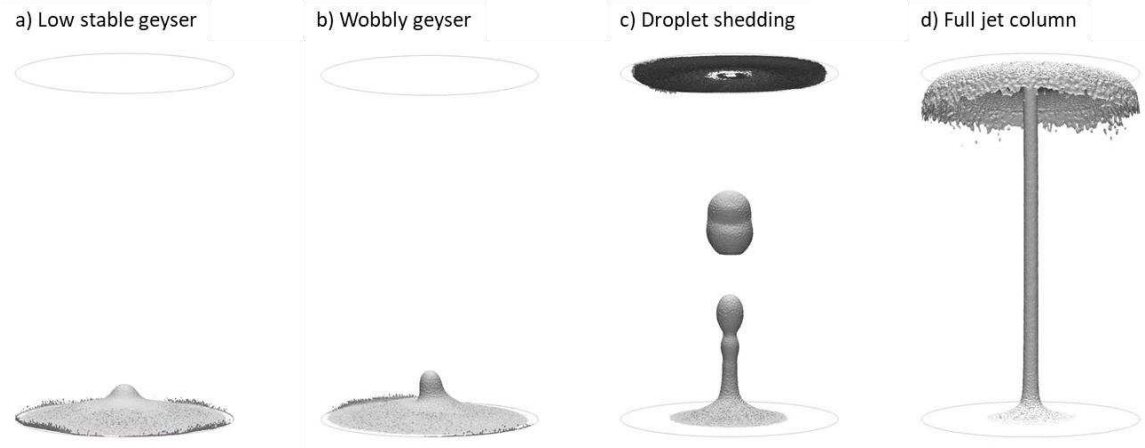


Figure 11 Four geyser patterns observed in the 3D models. The two stable geyser patterns are a) low stable geyser and b) wobbly geyser. The two unstable geyser patterns are c) droplet shedding and d) full jet column. Each example geyser shape is shown at approximately t = 4.5 seconds.

The black lines in Figure 12 and Figure 13 show the geyser interface at the center cross-section of the tank at a flow time of 9 seconds for a variety of inlet flow rates with a flat plug flow and a Poiseuille flow profile, respectively. As demonstrated in the figures, both the flow rate and the velocity profile affect the ultimate geyser shape. The stable geyser results are the 1.2 mL/s plug flow case (Figure 12a), which shows a low geyser shape, and the 1.4 mL/s plug flow (Figure 12b) and 1.0 mL/s Poiseuille flow cases (Figure 13a), which both display a wobbly geyser. The remaining cases have unstable geyser behaviors; the 1.2-1.4 mL/s Poiseuille flow cases (Figure 13b-d) show droplet shedding behavior, while the 1.65 mL/s Poiseuille flow case (Figure 13e) shows a full jet column.

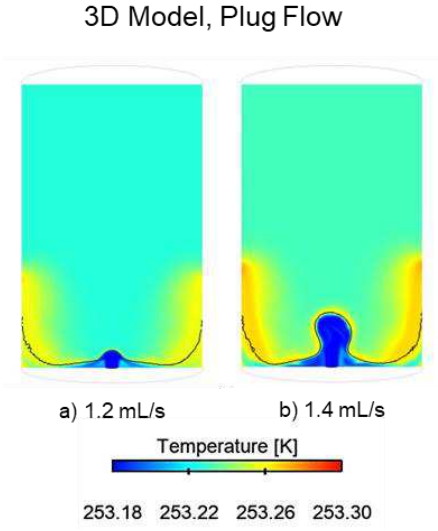


Figure 12 3D model with flat plug flow profile at 9 seconds flow time. Temperature contours of center plane with black line showing 0.5 liquid volume fraction.

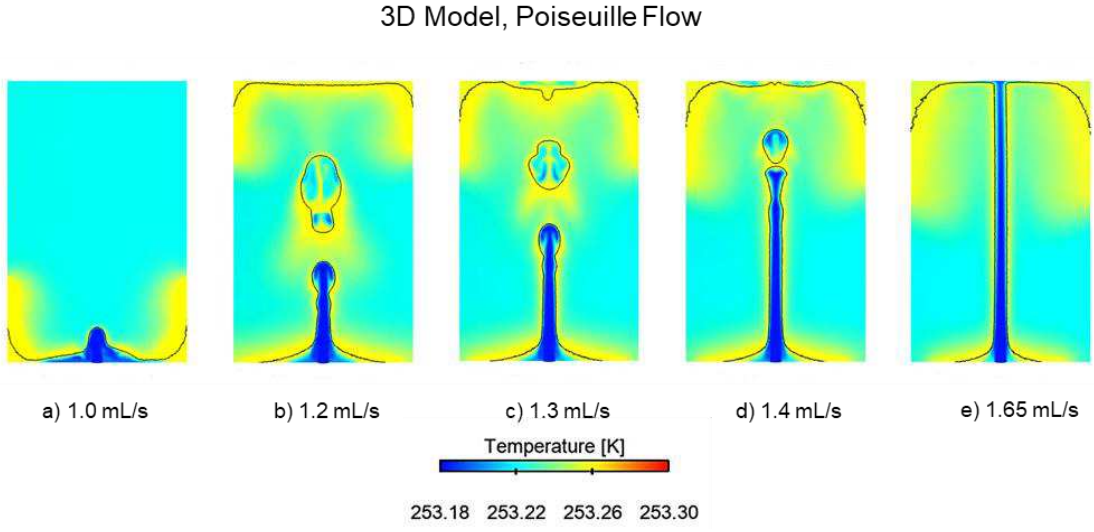


Figure 13 3D model with parabolic flow profile at 9 seconds flow time. Temperature contours of center plane with black line showing 0.5 liquid volume fraction.

10.2 3D Model Thermal Behavior and Pressure Evolution

The unvented filling of the tank causes thermal and pressure changes that can be evaluated in the model results. As liquid fills the unvented tank, the pressure begins to rise and some of the initial vapor in the tank starts to condense into liquid. Both the increase in tank pressure and the latent heat of condensation cause the tank temperature to rise. After the initial pressurizing phase, a quasi-stationary state is reached where the tank continues to fill, but the pressure remains largely steady. These phenomena are shown in Figure 12 to Figure 15.

Figure 12 and Figure 13 show the temperature colormaps at a flow time of 9 seconds for a variety of inlet flow rates with a flat plug flow and a Poiseuille flow profile, respectively. The bulk of the incoming liquid remains at or near the cold initial temperature, while the region near the liquid/vapor interface exhibits the hottest local temperatures due to the release of latent heat during condensation. The stable geyser shapes (Figure 12a-b and Figure 13a) have smaller interfacial surface areas, and a large amount of the local heating occurs at the tank side walls where the liquid rises due to capillary forces. These locations provide a favorable condensing surface without resupplying cold liquid from the incoming jet to distribute the latent heat generated. The unstable geyser shapes (Figure 13b-e) have comparatively more interfacial area, and thus experience more distributed local heating.

The plots in Figure 14 show vapor pressure (left) and phase change mass transfer (right) over time for the range of flow rates; the 3D Poiseuille flow model results (solid lines) are compared to the 0D thermodynamic model predictions (dashed lines). The 3D models follow the thermodynamic mass transfer curves closely for all the flow rates throughout the run, with higher flow rates yielding more heat transfer. Note that in the mass transfer plot, condensation is represented by negative mass transfer, so a more negative number means more condensation.

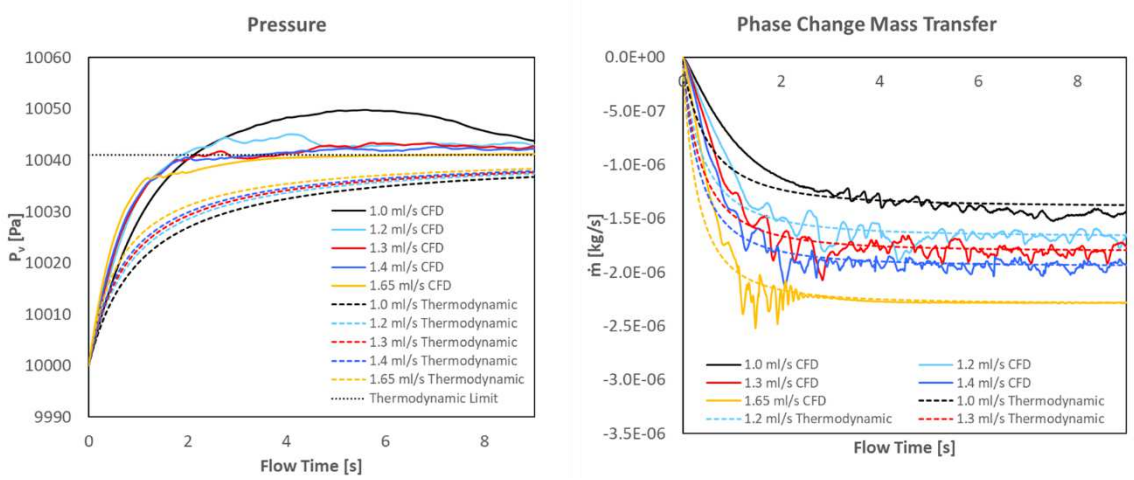


Figure 14 Vapor pressure (left) and mass transfer rate (right) as a function of time. Results of 3D model with parabolic flow profile are compared to thermodynamic model results and the thermodynamic pressure limit ($t \rightarrow \infty$).

The CFD pressures can be compared to the corresponding thermodynamically predicted pressure limits as time approaches infinity (dotted line). Pressure in the 3D models quickly rises and reaches a plateau at the thermodynamic limit, suggesting that these cases reach their quasi-stationary state faster than predicted by the thermodynamic solution. In some of the cases, particularly the 1.0 mL/s Poiseuille case, the pressure initially overshoots the thermodynamic limit before leveling off at the thermodynamic limit later in the simulation run. It is notable that the lowest flow rate shows the highest transient pressure peak. This demonstrates that a slower filling rate is not necessarily an effective strategy to prevent over-pressurizing of the tank during filling. It also shows an important discrepancy with the thermodynamic model, which is unable to predict transient pressure peaks and broadly suggests that a lower fill rate will always result in a lower early tank pressure. Despite the thermodynamic model's inability to capture transient behavior, the 9-second pressure values for all of the CFD models show strong agreement with the infinite-time pressure predicted by the thermodynamic model.

Figure 15 compares the 3D Poiseuille and plug flow results. The 1.2 mL/s plug flow case, the 1.4 mL/s plug flow case, and the 1.0 mL/s Poiseuille case all have stable geysers and show the highest transient pressure peaks in the plot; the remaining 3D Poiseuille cases have unstable geysers and show little to no pressure peak above the thermodynamic limit. The results suggest that the larger transient pressure peak in the stable geyser cases results directly from the geyser behavior shown in these cases, which is not captured by the thermodynamic model. The stable geyser shapes shown in Figure 12a-b and Figure 13a produce smaller interfacial area and less effective heat transfer from the vapor to the liquid phase compared to the droplets and jets in the unstable geyser cases shown in Figure 13b-e. This difference in interfacial areas provides a plausible mechanism for the dependence of the transient pressure on geyser stability, making the specific geyser flow behavior a crucial part of understanding an unvented filling system as a whole.

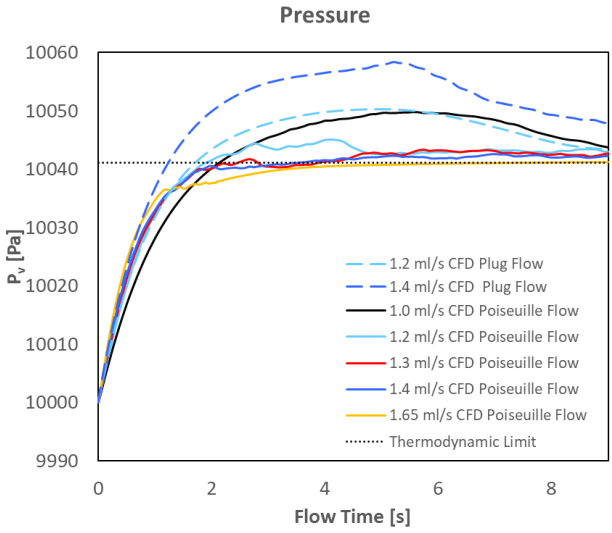
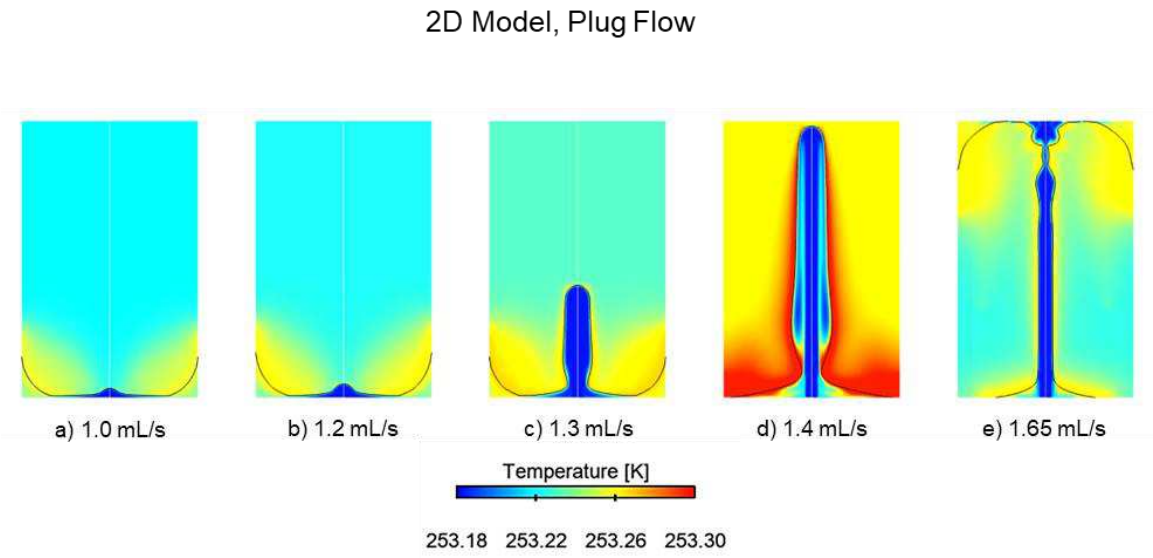


Figure 15 Vapor pressure as a function of time. Results of 3D model with both plug flow and parabolic flow profiles.

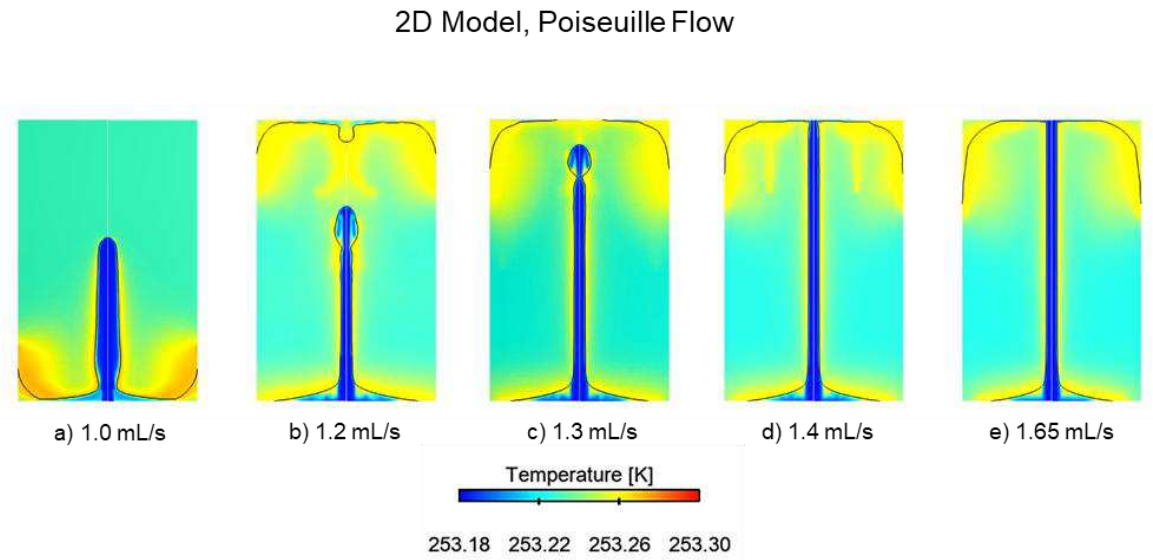
10.3 2D Axisymmetric Model Results

The 2D axisymmetric plug flow and Poiseuille flow results are shown in Figure 16 and Figure 17 as temperature colormaps at the center cross section of the tank. These cases correspond to the same range of inlet flow rates and conditions as the 3D results in Figure 12 and Figure 13. As in the 3D case, 1.0-1.2 mL/s plug flow shows a low geyser behavior, and 1.65 mL/s Poiseuille flow shows a full jet. The 2D axisymmetric models for 1.2-1.3 mL/s Poiseuille flow demonstrate less droplet detachment than the corresponding 3D results, and the 2D axisymmetric 1.4 mL/s Poiseuille flow case shows a full jet instead of droplet shedding.



480

481 **Figure 16** 2D axisymmetric model with flat plug flow profile at 9 seconds flow time. Temperature contours of
482 center plane with black contour line showing 0.5 liquid volume fraction.



483

484 **Figure 17** 2D axisymmetric model with parabolic Poiseuille flow profile at 9 seconds flow time. Temperature
485 contours of center plane with black contour line showing 0.5 liquid volume fraction.

486 The 1.0 mL/s Poiseuille case and the 1.4 mL/s plug flow case are found to be the least conducive for 2D
487 axisymmetric modeling. The asymmetric wobbly geyser behavior exhibited in the 3D model for these cases (Figure
488 13a and Figure 12b) cannot be captured in a 2D axisymmetric scheme. The corresponding 2D axisymmetric cases
489 (Figure 17a and Figure 16d) instead predict a necking liquid column shape and a large transient temperature rise.
490 Figure 18 compares the 2D axisymmetric case (a) with the corresponding 3D case (b) at 3-, 6-, and 9-seconds flow
491 time for the 1.4 mL/s plug flow case. Figure 18a shows the non-physical necking behavior along with the
492 increasingly large temperature rise predicted by the axisymmetric model, while Figure 18b shows the more realistic
493 wobbly 3D behavior, which breaks symmetry and can therefore not be captured by the axisymmetric model. This
494 demonstrates the most significant limitation of the 2D axisymmetric model compared to the 3D model.

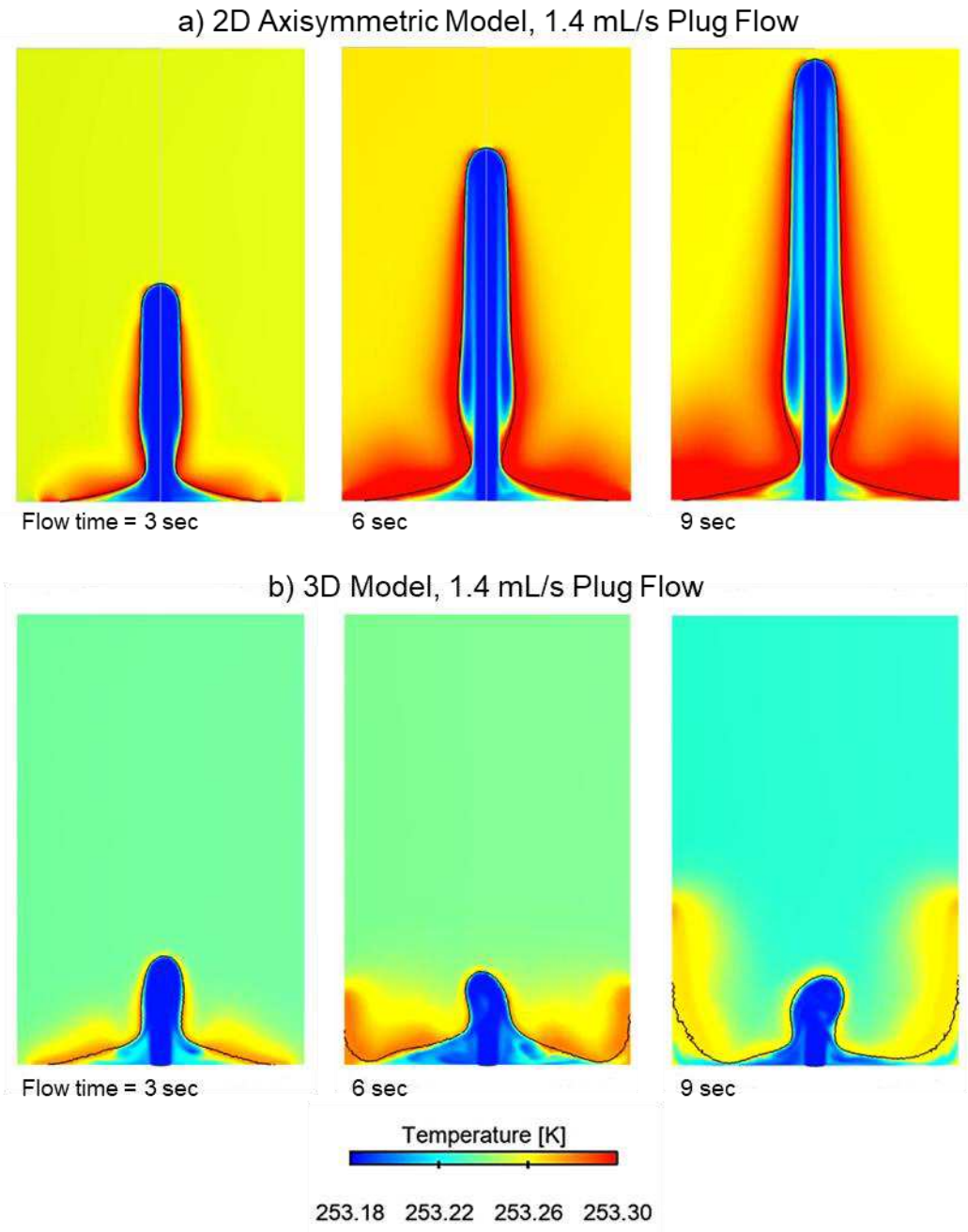


Figure 18 a) 2D axisymmetric model and b) 3D model with 1.4 mL/s flat flow profile. Temperature contours of center plane with black line showing 0.5 liquid volume fraction.

The limitation of the 2D axisymmetric model in predicting geyser behavior also affects the transient pressure evolution. Figure 19 shows vapor pressure (left) and phase change mass transfer (right) over time for the 2D axisymmetric and 3D 1.4 mL/s plug flow cases. The large non-physical temperature rise shown in the 2D axisymmetric case in Figure 18 also results in a more significant transient pressure rise, a longer time before the pressure returns to meet the thermodynamic limit, and a larger early condensation rate than is seen in the equivalent 3D case. This demonstrates the importance of the geyser behavior in predicting the transient pressure behavior of the tank.

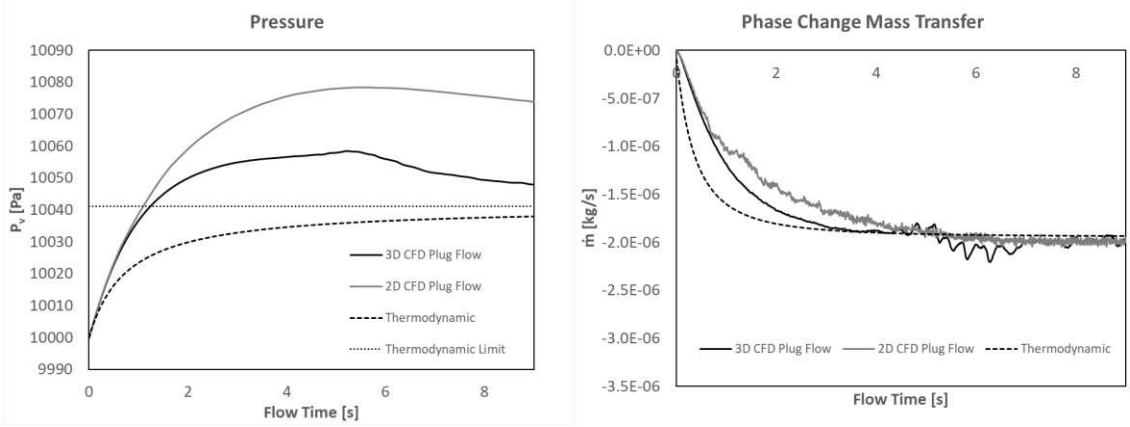


Figure 19 Vapor pressure (left) and mass transfer rate (right) as a function of time for 1.4 mL/s flat flow profile. Results of 3D model, 2D axisymmetric model, thermodynamic model and the thermodynamic pressure limit (t→∞) are shown.

10.4 Comparison Against Previous Experiments

Geyser patterns similar to those shown in the 3D model results presented here have also been observed in experimental studies of the low gravity filling problem. Images from two such experimental studies are shown in Figure 20. Figure 20a-c and Figure 20e-g are adapted from figure 16 of Govindan and Dreyer (2023), where a partially prefilled vented tank is filled at low gravity with HFE-7500 at flow rates from 1.1 mL/s to 1.5 mL/s, imaged at t = 9 sec. Figure 20d and h are adapted from figure 6 of Symons et al (1968), where an initially unfilled vented tank is filled at low gravity with trichlorotrifluoroethane at inlet velocities d) 9.95 cm/s and h) 13.9 cm/s, and imaged at t = <1 sec, 1.4 sec, and 2.1 sec (left to right). Figure 20a and b show low geyser behavior, while Figure 20c and d show wobbly geyser behavior. Figure 20e, f, and h all show droplet shedding behavior with various geyser lengths before droplet breakup, while Figure 20g depicts a full jet column.

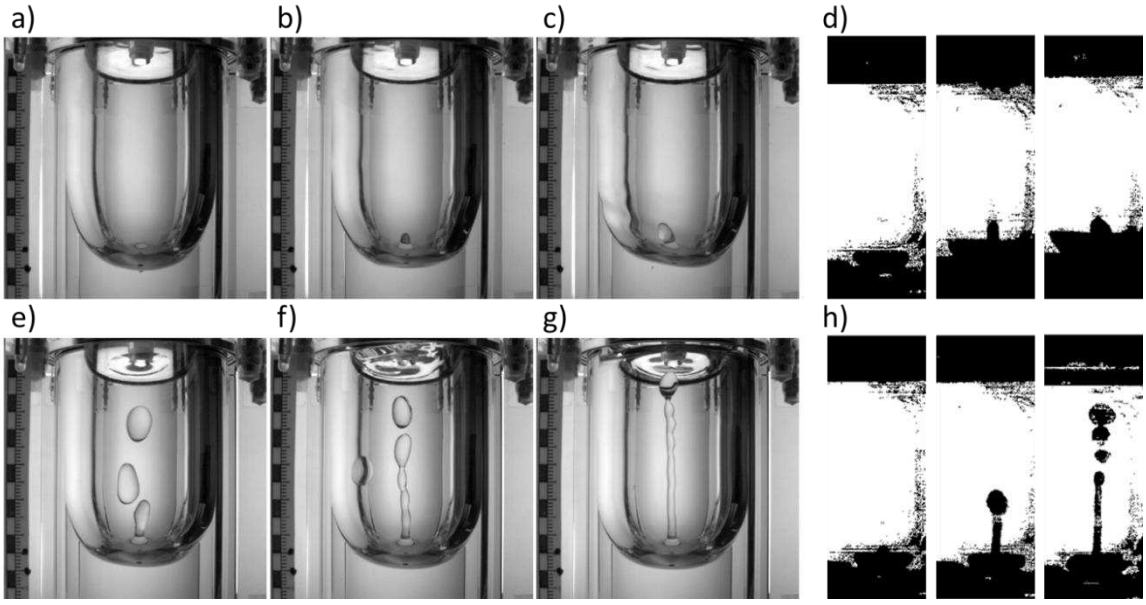


Figure 20 Previous experimental drop tower results showing stable (top row) and unstable (bottom row) geyser behaviors. a-c and e-g) From Govindan and Dreyer (2023) figure 16, partially prefilled tank with HFE-7500 at flow rates from 1.1 mL/s to 1.5 mL/s imaged at t = 9 sec. d and h) From Symons et al (1968) figure 6, initially unfilled tank with trichlorotrifluoroethane at inlet velocities d) 9.95 cm/s and h) 13.9 cm/s, and imaged at t = <1 sec, 1.4 sec, and 2.1 sec (left to right).

Aydelott (1979) also identified four geyser patterns for the case of partially filled tanks. In that work, Pattern I shows no disturbance of the liquid surface because the momentum of the incoming liquid is dissipated by the existing bulk liquid in the tank. In Pattern II, a stable geyser forms at the liquid surface without reaching the opposite end of the tank. In the final patterns, the geyser reaches the opposite tank wall and either pools at the opposite end of the tank wall in Pattern III or flows back along the walls to the bulk fluid in Pattern IV. Pattern I is not possible for an initially empty tank, as there is no existing bulk liquid to dissipate momentum. Pattern II represents a stable geyser condition, which is separated here into either a low stable geyser (Figure 11a) or a wobbly geyser (Figure 11b). There is not a clear distinction between Patterns III and IV for an initially empty tank, as there is no bulk liquid to flow back into, however these patterns are comparable to the full jet seen here in Figure 11d. The observation of droplet breakup, as seen here in Figure 11c, was only described in one Earth gravity test from Aydelott (1979) and was classified with Pattern IV, however the author notes that the droplets increased mixing in the bulk liquid compared to other tests.

10.5 Weber Number and Phase Mapping

Previous studies (Symons et al 1968; Symons 1969; Bentz et al 1997) have found the Weber number effective in characterizing the geyser behavior for a filling tank problem. The relevant Weber number for an initially empty tank is defined by Symons and Staskus (1971) as follows.

$$We = \frac{\int_{r=0}^{R_i} \rho_L \left[2\pi r \, dr \, v_i(r)\right] v_i(r)}{2\pi R_i \sigma_{LV}} = C \frac{\rho_L v_{i,avg}^2 R_i}{\sigma_{LV}} \tag{14}$$

The coefficient C is equal to ½ for a uniform flow profile and ⅔ for parabolic flow profile. Since it is likely that the experiments performed by Symons et al (1968) had a flow profile between a uniform profile and a fully developed parabolic flow profile, they were assigned a C value of 7/12 by Symons and Staskus (1971). The resulting data showed a critical Weber number of approximately 1.5; experiments below We = 1.5 displayed stable jet behavior, with no droplet detachment and a liquid geyser that remained close to the tank inlet wall without reaching the opposite side of the tank, while experiments above We = 1.5 displayed unstable jet behavior, with either droplet detachment or a full jet reaching the opposite side of the tank.

The phase map in Figure 21 shows the Weber number against the maximum inlet velocity for the unvented CFD simulations discussed in Sections 10.1 and 10.3, as well as for the experimental data from Symons et al (1968). Filled symbols in the plot denote stable behavior, while open symbols denote unstable behavior. The 1.4 mL/s plug flow and 1.0 mL/s parabolic flow cases are assigned as stable because their 3D results show a stable wobbly geyser behavior, despite the axisymmetric 2D CFD results.

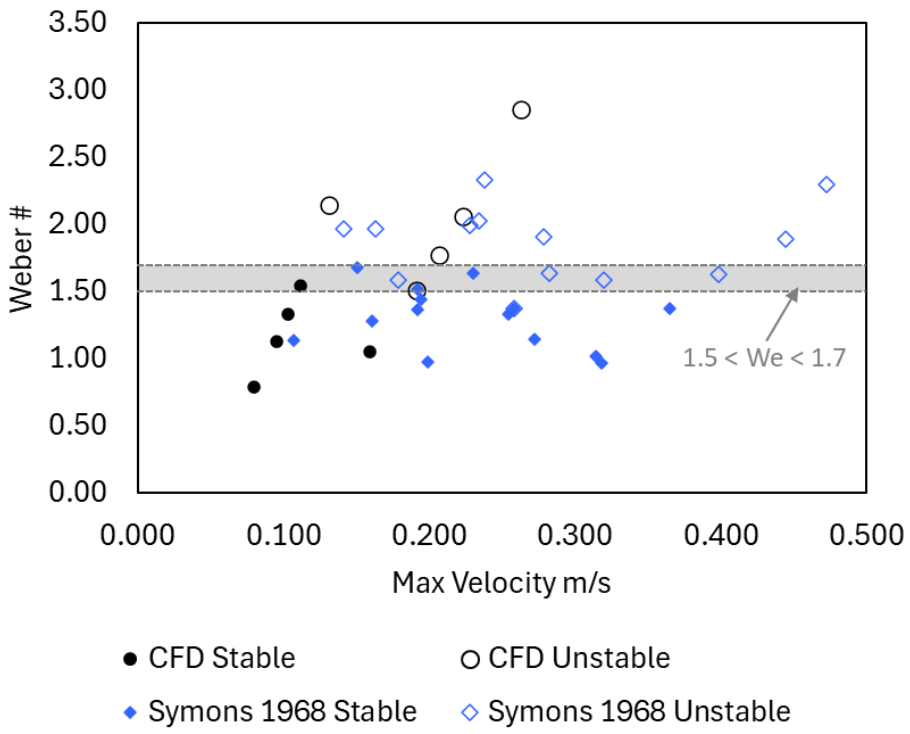


Figure 21 Phase map comparing the CFD results from this work to experimental data from Symons et al (1968). Filled symbols denote stable behavior, while open symbols denote unstable behavior.

The experimental and CFD results plotted on the phase map both largely conform to the Symons and Staskus (1971) conclusion that a critical Weber number of about 1.5 divides the unstable and stable regimes. No unstable case in either the experimental or numerical sets has a Weber number below 1.5, and no stable case has a Weber number above 1.7, demonstrating that the Weber number can be used to broadly predict the geyser behavior in cases that are far enough away from the critical value. However, the stability is not universally consistent with Weber number for all results within the 1.5-1.7 range. For example, the 1.2 mL/s parabolic flow case has a Weber number of 1.51 and shows unstable droplet detachment, while the 1.4 mL/s uniform flow case has a larger Weber number of 1.54 and shows a wobbly stable geyser. This inconsistency points to the potential that an additional parameter may play a role in the stability of the geyser.

Additionally, the Weber number does not seem to reliably distinguish low stable geyser cases from wobbly geyser cases. Distinguishing these geyser modes would be useful for determining whether a 2D axisymmetric model could be used, since wobbly geyser cases cannot be modeled in 2D axisymmetric while low stable geyser cases can be modeled reasonably well in 2D axisymmetric.

When comparing different experiments and numerical simulations, many aspects of the studies may be different, such as tank geometry, liquid properties, flow rate, tank venting, gravity, and initial tank condition. It is important to consider which conditions are likely to affect the resulting geyser behavior, and in what ways. Liquid properties, flow rate, and inlet radius are directly included in the definition of the Weber number and were investigated directly by Symons et al (1968). However other parameters are not included in the definition of Weber number presented in Equation (14). In the following sections, the effects of several important factors on behavior of the geyser are considered and discussed to enhance our ability to predict behavior and shed light on the generalizability of the predictions.

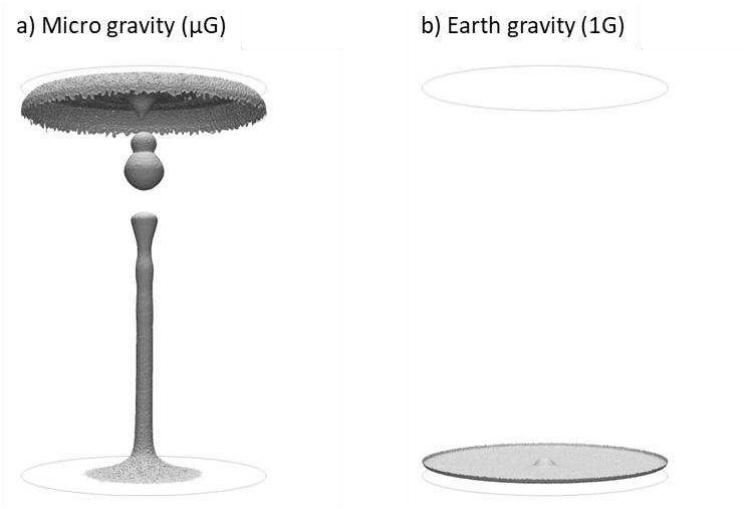
10.6 The Role of Gravity

The Weber number does not include gravity, however gravity is known to play an important role in geyser behavior. The Weber number indicates the relative strength of the capillary surface tension, which is the driving surface force

582 that determines the geyser stability and behavior in low and no gravity situations. In Earth gravity, however, the
583 gravitational body force plays a significant additional role in determining the geyser behavior.

584 The role of gravitational strength is explored in Figure 22. Figure 22a and b compare 1.4 mL/s Poiseuille flow cases
585 subjected to microgravity and Earth gravity, respectively. Unlike the droplet shedding behavior with the long
586 breakup height seen in microgravity conditions (Figure 22a), the Earth gravity case (Figure 22b) shows a low stable
587 geyser behavior even though both cases have a Weber number of 2.06. This occurs because, for an inlet at the
588 bottom of the tank, the gravitational body force on the geyser hinders the liquid's upward trajectory and creates
589 more stable geyser conditions.

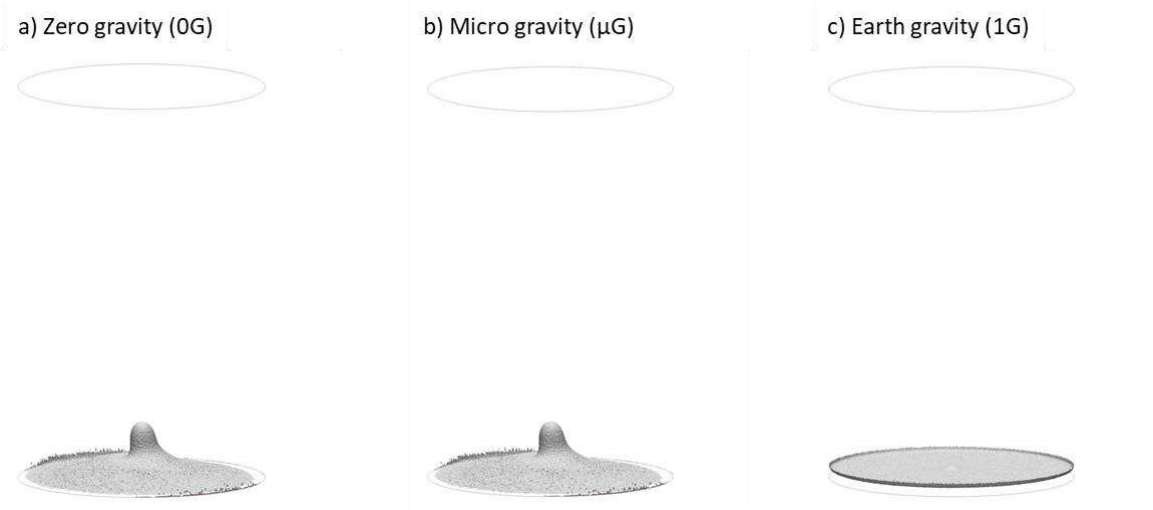
590 [Fig. 22 appears here]



591

592 **Figure 22** 3D shape of liquid interface at approximately t = 4.5 seconds for 1.4 mL/s parabolic flow profile with a)
593 microgravity and b) Earth gravity.

594 The same broad geyser behaviors seen in Figure 11 can be observed for high, low, or zero gravity conditions, though
595 the Weber number regimes where those behaviors are observed are dependent on gravitational conditions. For
596 example, Figure 23 demonstrates that the wobbly geyser behavior occurs at a low Weber number (We = 1.05) even
597 in the absence of gravity. This case shows a 1.0 mL/s Poiseuille flow no gravity case with the same wobbly stable
598 geyser behavior as the equivalent microgravity case in Figure 13, which is typical in drop tower experiments.

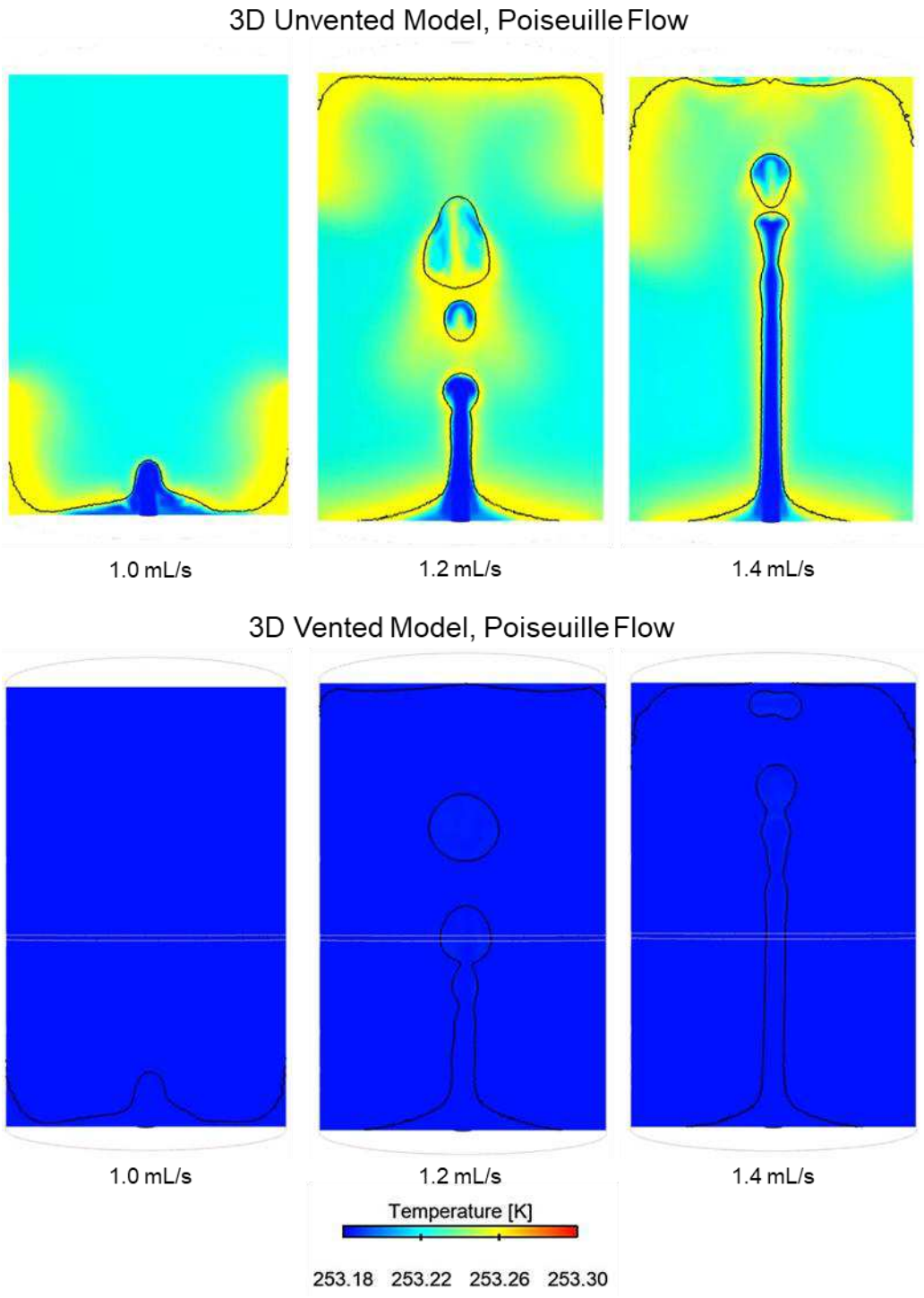


599

Figure 23 3D shape of liquid interface at approximately t = 4.5 seconds for 1.0 mL/s parabolic flow profile with a) zero gravity, b) microgravity, and c) Earth gravity.

10.7 Vented Tank Filling

Figure 24 compares the results of vented filling simulations for 1.0 mL/s, 1.2 mL/s, and 1.4 mL/s Poiseuille flow to their unvented counterparts. Venting allows vapor to escape the tank during filling, and thus prevents pressure rise in the tank. Without a rise in pressure, condensation phase change does not take place and temperature does not increase. The geyser shapes of the vented and unvented cases look similar for all flow rates. Slight differences in the individual droplet breakup for the 1.2 mL/s and 1.4 mL/s Poiseuille cases can be seen in Figure 24. The slight increase in breakup and coalescence of droplets in the unvented case is likely due to condensate that forms on the rising droplets.



610

611 **Figure 24** Unvented (top) and vented (bottom) 3D models with parabolic flow profile at 9 seconds flow time.
612 Temperature contours of center plane with black line showing 0.5 liquid volume fraction. Note that the vented tank
613 results in an isothermal temperature profile.

614 Different vent conditions are compared in Figure 25. Center plane temperature fields at 9 seconds are shown for the
615 unvented, top vented, and side vented 1.4 mL/s filling cases in Figure 25a, b, and c, respectively. Geyser behavior is
616 similar for all three cases, and the primary difference between the three cases is the extent of temperature rise. The

unvented case (Figure 25a) shows the largest temperature rise since no gas is able to leave the system. The side vented case (Figure 25c) is entirely isothermal, as gas can readily leave the system to keep the tank at a constant pressure and temperature. In the top vented case (Figure 25b), some gas can leave the tank, but the liquid partially obstructs the vent. This causes some notable temperature change in the system, which is most pronounced at interfaces where phase change occurs.

[Fig. 25 appears here]

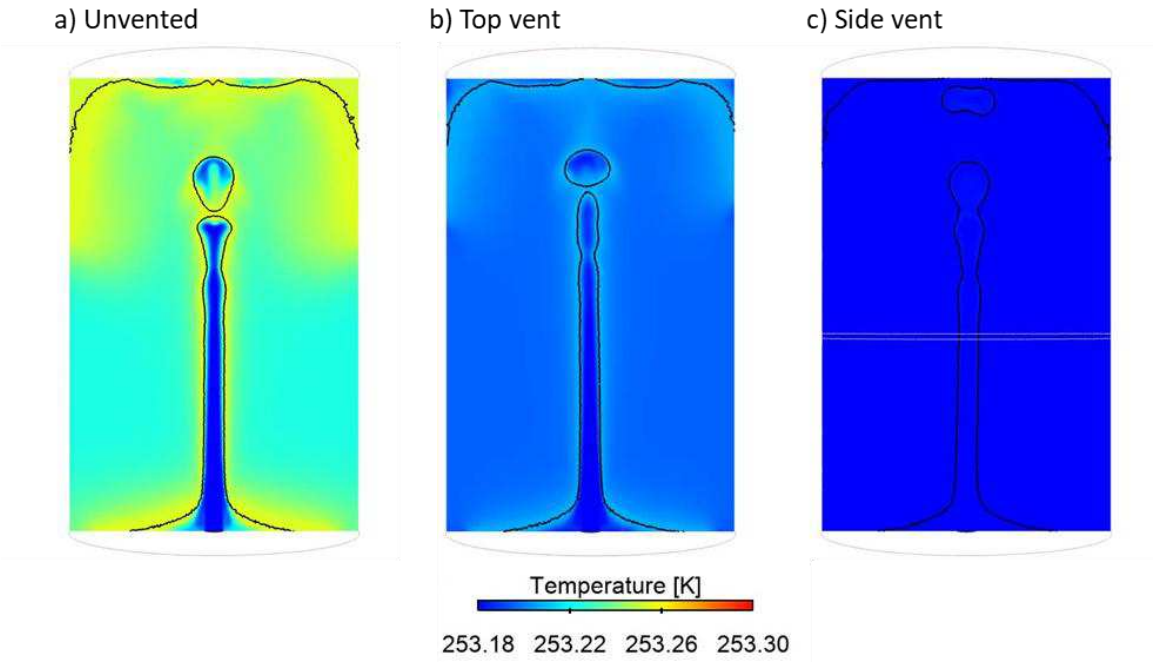


Figure 25 Temperature fields of center plane with black contour line showing 0.5 liquid volume fraction for the a) unvented, b) top vented, and c) side vented 1.4 mL/s tank filling cases.

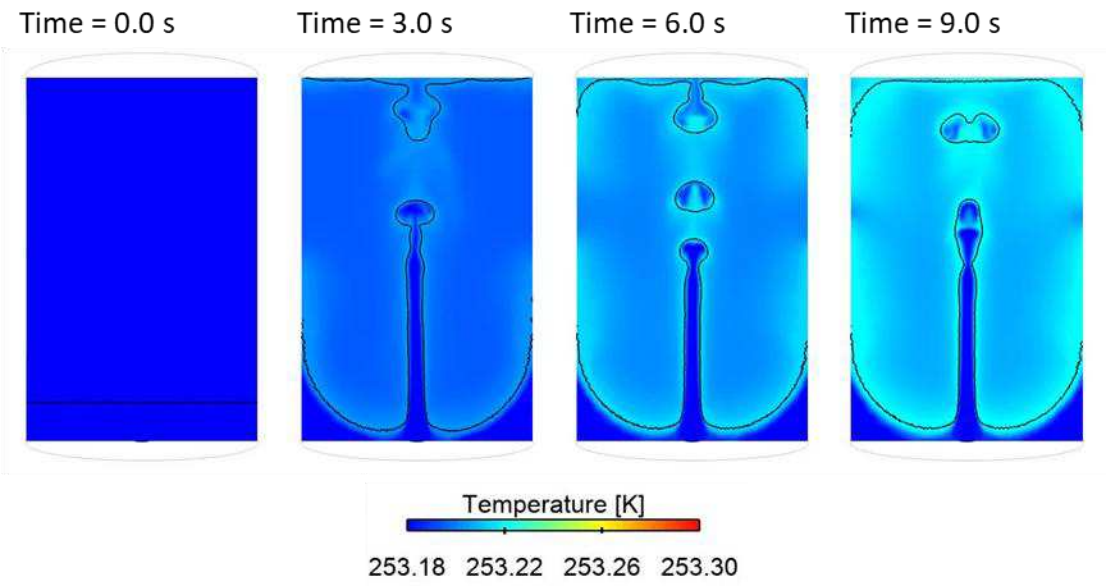
The results show why vented cases cannot be used to predict the thermal behavior or pressure evolution in an unvented tank. A partially vented tank will experience some temperature rise in the same general locations as its unvented tank counterpart, but the extent of the temperature rise is significantly lower.

The results further suggest that while individual droplet breakup may be slightly affected by the presence of phase change, this is unlikely to impact the overall geyser behavior and stability. Thus, geyser stability for vented and unvented cases can be treated as nearly the same and largely independent of the temperature developments in the tank.

10.8 Initial Tank Fill Condition

10.8.1 Partially Prefilled Tank

Refilling propellant tanks or tank top-offs typically occur before the tank is completely emptied. The case shown in Figure 26 is designed to simulate this condition, so it is given an initial liquid fill level of 10 mm from the bottom of the tank. The unvented filling proceeds at a rate of 1.4 mL/s. Compared to the initially gas-only filling case, the partially prefilled case has similar geyser behavior, with a similar breakup height and breakoff droplet size. The partially prefilled tank has been studied previously (Symons 1969; Symons and Staskus 1971; Bentz et al 1997), and an alternate formulation of the Weber number has been developed by Symons and Staskus (1971) to account for liquid jet spread as it travels through the prefilled liquid.



642

643 **Figure 26** Temperature fields of center plane with black contour line showing 0.5 liquid volume fraction for the
644 partially filled unvented 1.4 mL/s tank filling case.

645 Figure 26 shows that the partially filled case has a smaller temperature rise than the initially unfilled case in Figure
646 14d due to reduced condensation phase change. This suggests that the tank thermal behavior is also affected by the
647 initial tank fill level. The role of initial liquid height on the thermal and pressure evolution in an unvented filling
648 tank would be a worthwhile topic for future study.

649 **10.8.2 Vacuum Tank Filling**

650 In tank-to-tank transfer operations in space, the receiver tank is sometimes filled from an initially vacuum or near-
651 vacuum state, as opposed to the cases presented previously, where the tank initially contained vapor or a
652 combination of liquid and vapor at saturation conditions. To study the filling behavior of an empty tank in
653 microgravity, a model of an initially near-vacuum tank was constructed with the initial tank pressure set to 100 Pa, a
654 liquid filling flow rate of 1.4 mL/s, and a Poiseuille inlet velocity profile. The results of this near-vacuum case are
655 shown in Figure 27 and Figure 28, with corresponding pressure and mass transfer plots shown in Figure 29. Note
656 that the temperature color scale in Figure 28 is not consistent with previous figures because of the more dramatic
657 temperature changes in this case. At the beginning of the case (0-5 seconds), the liquid that enters the tank
658 undergoes flash vaporization (see Figure 27), and the liquid is seen evaporating rapidly and increasing the vapor
659 pressure in the tank (Figure 29 left). There is also significant cooling during this period (see Figure 28) due to the
660 extensive evaporation, which is shown in Figure 29 right. After the tank reaches a pressure of roughly 9000 Pa, the
661 pressure begins to level off (Figure 29 left) and evaporation drops considerably (Figure 29 right). As the simulation
662 continues (5-15 seconds), the vapor pressure builds more slowly in Figure 29 left and small liquid droplets scatter
663 throughout the tank in Figure 27 without a true geyser at the center. Figure 29 shows that when the tank pressure
664 reaches approximately 9500 Pa, condensation begins to outpace evaporation in the tank. Once the simulation reaches
665 a flow time of approximately 30 seconds, the tank temperature shown in Figure 28 rises to approach the temperature
666 of the entering liquid, and the vapor pressure in the tank (9860 Pa, see Figure 29 left) is large enough to support a
667 liquid geyser. This geyser seen in Figure 27 and Figure 28 begins to resemble the geyser behavior in the 3D 1.4
668 mL/s cases discussed in Section 10.1. This suggests that while the thermal behavior is different, the liquid geyser
669 behavior predicted in the previous cases may be applicable to initially vacuum cases after the early flash evaporation
670 phase.

671 [Fig. 27 appears here]

672 [Fig. 28 appears here]

[Fig. 29 appears here]

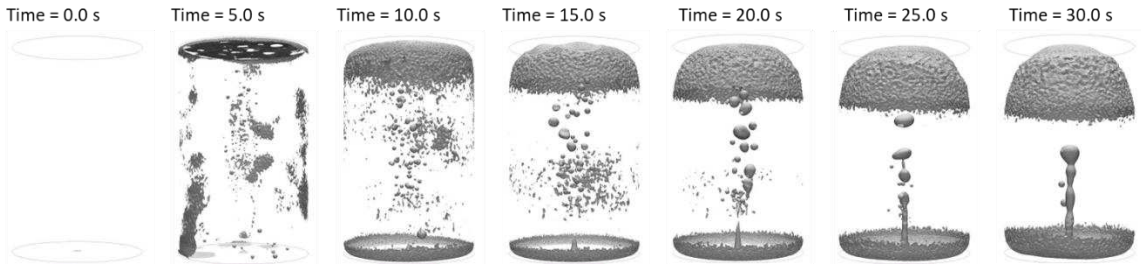


Figure 27 3D shape of liquid interface for the vacuum 1.4 mL/s filling case over time.

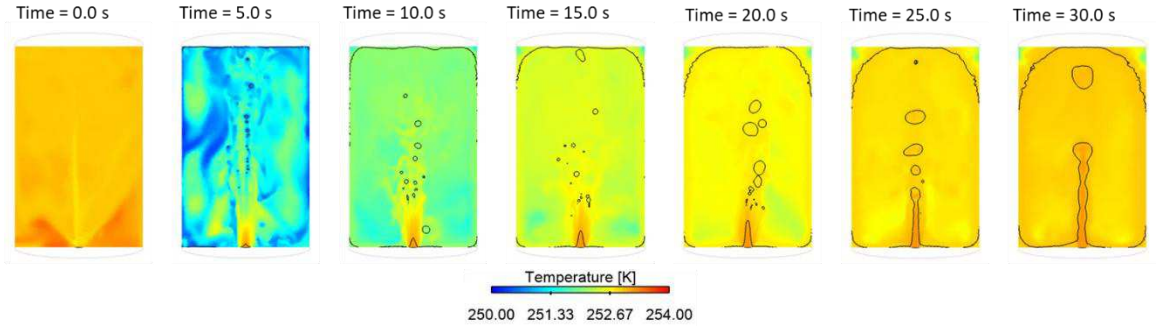


Figure 28 Temperature contours of the center plane for the vacuum 1.4 mL/s filling case over time. The black lines indicate liquid fraction of 0.5. Note that the temperature color scale is not consistent with previous figures.

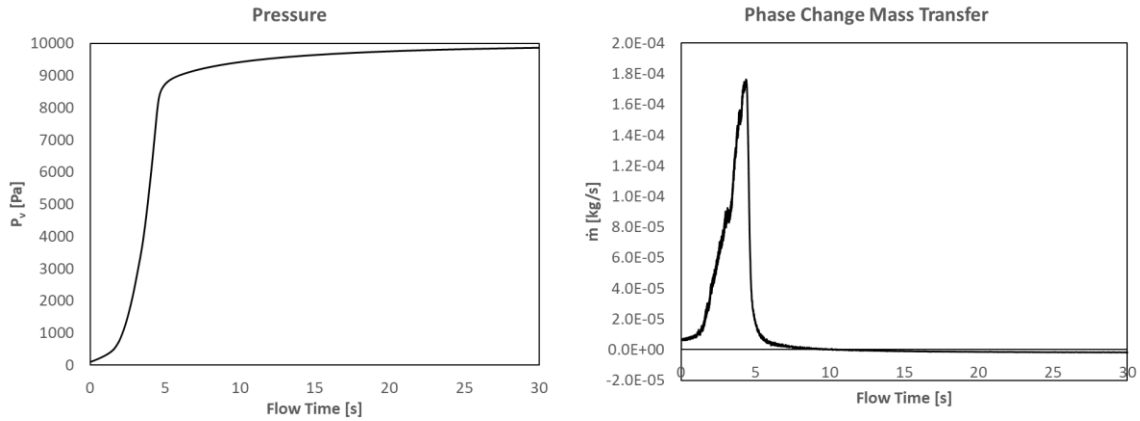


Figure 29 Vapor pressure (left) and mass transfer rate (right) as a function of time for vacuum 1.4 mL/s filling case.

11 Conclusion

2D-axisymmetric and 3D CFD models, as well as a 0D thermodynamic model, were developed for simulating vented and no-vent tank fillings in microgravity. These simulations provide better understanding of the intricate physics of the geyser and phase change behavior and predict the tank pressure during filling. In the 3D CFD model, the geyser behavior spans different regimes based on the filling flow rate and velocity profile at the inlet. The behaviors from low to high inlet velocity are a low geyser that barely penetrates a slowly filling bottom tank wall, a wobbly geyser that tilts erratically around the centerline, a line of droplets that reach to the opposite wall of the tank (droplet breakup), and a full unbroken jet from the inlet to the opposite wall. The models suggest that geyser behavior significantly affects the presence and size of an early spike in the tank pressure during initial filling. Specifically, stable geyser cases displayed the highest transient pressure peaks while unstable geyser cases often displayed little to no pressure peak due to the increased surface area in these geyser patterns. This finding suggests

692 that a lower fill rate does not always result in a lower transient tank pressure, particularly when the fill rate reduction
693 results in a transition from unstable to stable geyser regime. This emphasizes the importance of understanding the
694 fluid behavior for accurately capturing the pressure evolution in unvented tank filling.

695 The 2D, 3D, and thermodynamic models showed broad agreement in final pressure and mass transfer. As expected,
696 the thermodynamic model did not capture the early transient pressure overshoot and slow pressure reduction that
697 was seen in the CFD models. Compared to the 3D results, the 2D axisymmetric model demonstrated less overall
698 droplet breakup, as well as nonphysical behavior specifically for cases that exhibited an asymmetric wobbly stable
699 geyser in 3D.

700 Weber number adjusted for inlet velocity profile was found to broadly predict geyser stability, with a critical Weber
701 number of approximately 1.5 to 1.7, which is consistent with previous experimental findings. The level of gravity
702 present is known to play an important role in geyser behavior, as the gravitational force acts on the geyser to pull it
703 towards the bottom of the tank. However, no discernable differences in behavior were found between microgravity
704 and zero-gravity conditions, allowing for comparison to drop tower experimentation as well as prediction for future
705 low Earth orbit and deep space missions. The vented tank geyser behavior was nearly the same as that of the
706 unvented tank, with small differences in droplet breakup due to condensation at the geyser interface in the unvented
707 filling conditions. Meanwhile, the presence and location of a vent was found to impact the thermal evolution, as the
708 top vent was partially blocked by impinging liquid and allowed some temperature rise while the side vent resulted in
709 a completely isothermal case with no pressure rise. The initial fill condition of the tank was also found to impact
710 behavior. The partially filled no-vent tank filling simulation showed a reduced temperature rise compared to the
711 initially gas-only case. The near-vacuum no-vent tank filling began with flash evaporation and significantly different
712 behavior from the other cases. After roughly 30 seconds of flow time, the geyser behavior in this case began to
713 resemble that of the base filling case.

714 Inconsistency in geyser stability was found within the 1.5-1.7 range of Weber number, suggesting the possibility that
715 one or more additional parameters play a role in geyser stability. This study identifies the important role that geyser
716 stability and behavior play in the early pressure evolution of low gravity no-vent tank filling. Future work focused
717 on identifying all critical parameters would allow for better theoretical prediction of geyser stability.

718

12 References

J. C. Aydelott, Axial jet mixing of ethanol in cylindrical containers during weightlessness, Nr. NASA-TP-1487, NASA Lewis Research Center, 1979.

M. D. Bentz, J. M. Albayyari, R. H. Knoll, M. M. Hasan, and C. S. Lin, *Tank pressure control experiment: Results of three space flights*, 33rd AIAA/ASME/ SAE/ASEE Joint Propulsion Conference and Exhibit, Nr. AIAA-97-2816, AIAA, 1997.

S. R. Breon, R. F. Boyle, M. B. Francom, C. H. DeLee, J. J. Francis, S. Mustafi, P. W. Barfknecht, J. M. McGuire, A. G. Krenn, G. A. Zimmerli, and D. M. Hauser, *Robotic refueling mission-3—an overview*, IOP conference series: Materials science and engineering, 755(1), pp. 012002, 2020.

D. J. Chato, *Analysis of the non-vented fill of a 4.96-cubic-meter lightweight liquid hydrogen tank*, NASA Technical Memorandum 1020391989, 27th National Heat Transfer Conference, ASME, 1989.

D. J. Chato, Ground testing for the no-vent fill of cryogenic tanks: Results of tests for a 71 cubic foot tank, 29th Joint Propulsion Conference and Exhibit, Nr. AIAA-93-1967, AIAA, 1993.

D. J. Chato, Thermodynamic modeling of the no-vent fill methodology for transferring cryogens in low gravity, AIAA/ASME/SAE/ASEE 24th Joint Propulsion Conference, AIAA-88-3403, AIAA, 1988.

D. J. Chato and T. A. Martin, *Vented tank resupply experiment: Flight test results*, Journal of Spacecraft and Rockets, 43.5, pp. 1124-1130, 2006.

D. J. Chato and R. Sanabria, *Review and test of chilldown methods for space-based cryogenic tanks*, NASA Technical Memorandum 104458, AIAA-91-1843, 1991.

S. Dominick and S. Driscoll, *Fluid acquisition and resupply experiment (FARE I) flight results*, Proceedings of the 29th Joint Propulsion Conference, Nr. AIAA-93-2424, AIAA, 1993.

S. Dominick and J. Tegart, *Orbital test results of a vaned liquid acquisition device*, Proceedings of the 30th Joint Propulsion Conference, Nr. AIAA-94-3027, AIAA, 1994.

R. H. Flachbart, A. Hedayat, and K. A. Holt, Modeling and test data analysis of a tank rapid chill and fill system for the advanced shuttle upper stage (ASUS) concept, AIP Conference Proceedings, 613(1), pp. 1284-1291, 2002.

J. P. Gille, *Analysis and modeling of fluid transfer in orbit*, AIAA/ASME/ SAE/ASEE 22nd Joint Propulsion Conference, Nr. AIAA-86-1718, AIAA, 1986.

S. N. Govindan and M. E. Dreyer, Experimental investigation of liquid interface stability during the filling of a tank in microgravity, Microgravity Science and Technology, 35(3), 2023.

J. I. Hochstein, J. G. Marchetta, and R. J. Thornton, *Microgravity geyser and flowfield prediction*, Journal of Propulsion and Power, 24(1), pp.104-110, 2008.

S. C. Honkonen, F. O. Bennett Jr., and H. K. Hepworth, *An analytic model for low-gravity tank chilldown and no-vent fill: The general dynamics no-vent fill program (GDNVF)*, AIAA 26th Thermophysics Conference, Nr. AIAA-91-1380, AIAA, 1991.

O. Kartuzova and M. Kassemi, CFD jet mixing model validation against zero-boil-off tank (ZBOT) microgravity experiment, AIAA Propulsion and Energy, Nr. AIAA-2019-4282, AIAA, 2019.

O. Kartuzova and M. Kassemi, *Computational fluid dynamics analysis of jet-ullage interactions during microgravity mixing*, Journal of Thermophysics and Heat Transfer, 38(1), pp. 74-85, 2024.

O. Kartuzova and M. Kassemi, *Modeling K-Site LH2 tank chilldown and no vent fill in normal gravity*, AIAA-2017-4662, AIAA Propulsion and Energy Forum, 2017.

M. Kassemi and O. Kartuzova, Effect of interfacial turbulence and accommodation coefficient on CFD predictions of pressurization and pressure control in cryogenic storage tank, Cryogenics, 74, pp. 138-153, 2016.

M. Kassemi, O. Kartuzova, and S. Hylton, *Results of the microgravity zero-boil-off tank (ZBOT) experiment*, 69th International Astronautical Congress (IAC), Nr. IAC-18-A2.2.6-43028, IAF, 2018.

Y. Ma, Y. Li, K. Zhu, Y. Wang, L. Wang, and H. Tan, *Investigation on no-vent filling process of liquid hydrogen tank under microgravity condition*, International Journal of Hydrogen Energy, 42(12), pp. 8264-8277, 2017.

Y. Ma, Y. Zhang, X. Luo, Y. Li, and F. Xie, Analysis and modeling of no-vent filling process for liquid-hydrogen tank in orbital conditions, Processes, 11(5), pp.1315, 2023.

A. Majumdar, No vent tank fill and transfer line chilldown analysis by generalized fluid system simulation program (GFSSP), Thermal and Fluids Analysis Workshop, Marshall Space Flight Center, 2013.

J. G. Marchetta, and R. H. Benedetti, 2010. *Simulation of jet-induced geysers in reduced gravity.* Microgravity Science and Technology, 22(1), pp.7-16, 2010.

M. E. Moran, T. W. Nyland, and S. S. Papell, *Liquid transfer cryogenic test facility: Initial hydrogen and nitrogen no-vent fill data*, Nr. NASA-TM-102572, NASA Lewis Research Center, 1990.

M. E. Moran, T. W. Nyland, and S. L. Driscoll, *Hydrogen no-vent fill testing in a 1.2 cubic foot (34 liter) tank*, Technical Report NASA-TM-105273, NASA Lewis Research Center, 1991.

G. R. Schmidt, R. W. Carrigan, J. E. Hahs, D. A. Vaughan, and D. C. Foust, *No-vent fill pressurization tests using a cryogen simulant*, Nr. NASA TM-103561, NASA Marshall Space Flight Center, 1991.

E. P. Symons, Liquid inflow to partially full, hemispherical-ended cylinders during weightlessness, No. NASA-TM-X-1934, NASA Lewis Research Center, 1969.

E. P. Symons, R. C. Nussle, and K. L. Abdalla, *Liquid inflow to initially empty, hemispherical ended cylinders during weightlessness*, No. NASA-TN-D-4628, NASA Lewis Research Center, 1968.

E. P. Symons and J. V. Staskus, Interface stability during liquid inflow to partially full, hemispherical ended cylinders during weightlessness, Nr. NASA-TM-X-2348, NASA Lewis Research Center, 1971.

W. J. Taylor and D. J. Chato, Comparing the results of an analytical model of the no-vent fill process with no-vent fill test results for a 4.96 cubic meters tank, 28th Joint Propulsion Conference and Exhibit, Nr. NASA-TM-106018, NASA Lewis Research Center, 1992.

W. J. Taylor and D. J. Chato, Improved thermodynamic modeling of the no-vent fill process and correlation with experimental data, Nr. NASA-TM-104492, NASA Lewis Research Center, 1991.

D. A. Vaughan, D. C. Foust, and G. Schmidt, *Enhancement of the no-vent fill process*, AIAA/SAE/ASME/ASEE 27th Joint Propulsion Conference, Nr. AIAA-91-1842, AIAA, 1991.

D. A. Vaughan and G. R. Schmidt, *Analytical modeling of no-vent fill process*, Journal of Spacecraft and Rockets, 28(5), pp. 574-579, 1991.

C. Wang, Y. Li, and R. Wang, Performance comparison between no-vent and vented fills in vertical thermal-insulated cryogenic cylinders, Experimental Thermal and Fluid Science, 35(2), pp. 311-318, 2011.

L. Wang, Y. Z. Li, F. N. Zhang, and Y. Ma, Performance analysis of no-vent filling process for liquid hydrogen tank in terrestrial and on-orbit environments, Cryogenics, 7, pp. 55-61, 2015.

C. Wang and R. Wang, The effects of vertical and horizontal placement on no-vent fill of cryogenic insulated vessels, Cryogenics, 50, pp. 480-485, 2010.

13 Nomenclature

c_{pL}	Specific heat capacity of the liquid
c_{pV}	Specific heat capacity of the vapor
c_W	Specific heat capacity of the wall
h_{LV}	Enthalpy of vaporization
k	Thermal conductivity
$\dot{m}$, $\dot{M}$	Mass flow rate (can be either mass entering, mass exiting, or mass transfer due to phase change)
$\dot{M}_{IN}$	Total mass flow rate entering the system
$\dot{M}_{L,IN}$	Mass flow rate of liquid entering the system
$\dot{M}_{L,OUT}$	Mass flow rate of liquid exiting the system
$\dot{M}_{OUT}$	Total mass flow rate exiting the system
$\dot{M}_{V,IN}$	Mass flow rate of vapor entering the system
$\dot{M}_{V,OUT}$	Mass flow rate of vapor exiting the system
M_M	Molar mass of the fluid
M_W	Mass of the wall
P	Pressure
P_V	Pressure in the vapor
$\dot{Q}_W$	Heat transfer rate of heat entering the system through the wall
R	Universal gas constant
R_i	Inlet radius
r	Radial coordinate
S	Source term in governing equation
T	Temperature
T_{IN}	Temperature of the mass entering the system
t	Time
V_L	Liquid volume
V_T	Total tank volume
V_V	Vapor volume
v_i	Inlet velocity
$v_{i,avg}$	Average inlet velocity
α_L	Volume fraction of liquid
α_V	Volume fraction of vapor
θ	Contact angle
μ	Kinematic viscosity
ρ_L	Liquid density
ρ_V	Vapor density
σ_{acc}	Accommodation coefficient
σ_{LV}	Surface tension